ICARUS 115, 159–180 (1995)

The Rate of Pyrite Decomposition on the Surface of Venus

B. FEGLEY, JR. AND K. LODDERS

Department of Earth and Planetary Sciences, Campus Box 1169, Washington University, One Brookings Drive, St. Louis, Missouri 63130-4899
E-mail: bfegley@planet.win.net

A. H. TREIMAN

Lunar and Planetary Institute, 3600 Bay Area Boulevard, Houston, Texas 77058

AND

G. KLINGELHÖFER

Institut für Kernphysik, Technische Hochschule Darmstadt, Schlossgartenstrasse 9, D64289 Darmstadt, Germany

Received April 18, 1994; revised January 27, 1995

We report the results of a detailed experimental study of the kinetics and mechanism of pyrite (FeS_2) chemical weathering under Venus surface conditions. Pyrite is thermodynamically unstable on the surface of Venus and will spontaneously decompose to pyrrhotite (Fe_7S_8) because the observed S_2 partial pressure in the lower atmosphere of Venus is lower than the S_2 vapor pressure over coexisting pyrite and pyrrhotite. Pyrite decomposition kinetics were studied in pure CO_2 and CO_2 gas mixtures (CO–CO_2, Ar–CO_2, H_2–CO_2, CO–CO_2–SO_2) along five isotherms in the temperature range 390–531°C. In all gas mixtures studied, pyrite thermally decomposes to pyrrhotite (Fe_7S_8), which on continued heating loses sulfur to form more Fe-rich pyrrhotites. During this process the pyrrhotites are also being oxidized to form magnetite (Fe_3O_4), which converts to maghemite (γ-Fe_2O_3), and then to hematite (α-Fe_2O_3). This reaction sequence is supported by X-ray diffraction data, Mössbauer spectra, optical microscopy, and prior literature studies. The reaction rates for pyrite thermal decomposition to pyrrhotite were determined by measuring the weight loss. The thickness of the unreacted pyrite in the samples provided a second independent reaction rate measurement. Finally, Mössbauer spectra done on 42 of the 115 experimental samples provided a third set of independent reaction rate data. All three independent methods give the same reaction rate within experimental uncertainties. Pyrite decomposition follows zero-order kinetics and is independent of the amount of pyrite present. The rate of pyrite decomposition is apparently independent of the gas compositions used and of the CO_2 number density over a range of a factor of 40. The derived activation energy of ~150 kJ mole^{-1} is the same in pure CO_2, two different CO–CO_2 mixtures, and a ternary CO–SO_2–CO_2 mixture. Based on data for a CO–CO_2–SO_2 gas mixture with a CO number density ~10 times higher than at the surface of Venus and a SO_2 number density approximately equal to that at the surface of Venus, the rate of pyrite destruction on the surface of Venus varies from about 1225 ± 238 days/cm at the top of Maxwell Montes (~660 K) to about 233 ± 133 days/cm in the plains of Venus (~740 K). These lifetimes are very short on a geological time scale and show that pyrite cannot exist on the surface of Venus for any appreciable length of time.

INTRODUCTION

Over a decade ago, data from the Pioneer Venus spacecraft, the Venera 11/12 spacecraft, and Earth-based remote sensing were used to propose a theoretical model for the sulfur geochemical cycle on Venus (Von Zahn *et al.* 1983; Prinn 1985). Figure 1 illustrates a modified version of the sulfur geochemical cycle proposed at that time. It shows the gas phase, gas–aerosol, and gas–rock reactions which continuously cycle sulfur among the atmosphere of Venus, the clouds of Venus, and rocks on the surface of Venus.

An important component of the sulfur geochemical cycle is pyrite chemical weathering, which was predicted to be a source of reduced sulfur gases at the surface of Venus. After the Pioneer Venus and Magellan missions, pyrite was also proposed to be present in low-emissivity regions in the highlands of Venus (Pettengill *et al.* 1982, 1988, 1991). The pyrite model to explain low-emissivity regions on Venus was accepted by a large number of planetary scientists. However, as shown by Fegley and Treiman (1992), pyrite is thermodynamically unstable on the surface of Venus and will spontaneously decompose to pyrrhotite (Fe_7S_8).

Because of the great interest in the geochemistry of

0019-1035/95 $6.00

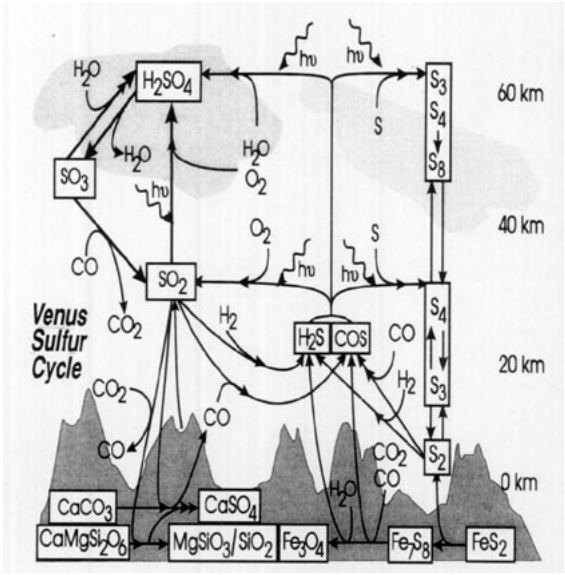

FIG. 1. A modified version of the Venus sulfur cycle proposed by Von Zahn *et al.* (1983) and Prinn (1985). Our experimental results showing that anhydrite ($CaSO_4$) is formed from SO_2 reacting with Ca minerals (Fegley and Prinn 1989) and our results showing the pyrite → pyrrhotite → Fe oxide reaction sequence are incorporated into this diagram.

pyrite on Venus we made an experimental study of pyrite decomposition under Venus-like temperatures and compositions (Fegley and Treiman 1991; Fegley and Lodders 1993a,b; Fegley *et al.* 1993; Klingelhöfer *et al.* 1994). The results of our study lead to a modified version of the sulfur geochemical cycle on Venus and show that pyrite rapidly decomposes over the entire surface of Venus. Furthermore, the experimental data are important for models of venusian geochemistry, for models of sulfur chemistry in the lower atmosphere of Venus, for studies of the origin and evolution of the atmosphere of Venus, for the design of future spacecraft missions to Venus, and for the rapidly evolving Earth-based IR observations of the subcloud atmosphere of Venus.

EXPERIMENTAL KINETIC STUDIES

Pyrite thermal decomposition was studied in two different series of experiments. One series was done in Treiman's former laboratory at Boston University (BU), and another series was done in Fegley's laboratory at Washington University, St. Louis (WU). About 130 experiments (115 at WU and 16 at BU) were done to determine the effects of temperature, gas partial pressures, and oxygen fugacity on the pyrite decomposition rate. Pyrites from different geographical locations and different geological settings (e.g., hydrothermal and magmatic deposits) were used in the experiments to see whether different types of pyrite decomposed at different rates. These studies showed no difference between the different pyrite samples and no effect of the minor impurities. The experiments used standard techniques that have been developed in materials science for studying gas–solid reactions (e.g., Kubaschweski *et al.* 1993; Schwertdfeger and Turkdogan 1970).

Starting Materials

Single crystal cubes (1 cm on a side) from a felsic schist (locality unknown, Boston University collection) and single crystal cubes (2 cm on a side) from a chlorite schist at the Carlton talc deposit in Chester, VT (Gillson, 1927; Harvard Mineralogical Museum Catalog 122623) were used in the runs at BU. Experiments carried out at Washington University utilized pyrite cubes (2.5 cm on a side) from Navajun, Spain, which are found in marl (Calvo and Sevillano 1989), and magmatic pyrite from Huanzala, Peru. All four pyrite samples have X-ray diffraction (XRD) patterns identical to that of pyrite (JCPDS pattern 42-1340). Three replicate gravimetric analyses of the Peruvian pyrite, done by heating inclusion-free pieces in air at 1100°C, gave a Fe/S atomic ratio of 2.0004 ± 0.0004 (1 σ error). The oxidation product showed only hematite lines in the X-ray diffraction pattern. Gravimetric analysis of the Spanish pyrite, which contains some inclusions, showed that it is 97% pure with 3% of other material. Instrumental neutron activation analysis (INAA) of the Spanish pyrite gave 45.43 ± 1.36 mass% Fe vs 46.55% for FeS_2, corresponding to 98% purity, in agreement with the gravimetric data. A similar result was obtained from INAA of the BU pyrite. Electron microprobe analyses of inclusion-free areas of the Spanish pyrite are identical to stoichiometric FeS_2 within analytical uncertainties (Fe = 46.60 ± 0.16 mass% and S = 54.01 ± 0.34 mass% vs 46.55% and 53.45%, respectively, for stoichiometric FeS_2). Mössbauer spectroscopy of unreacted samples of the Spanish and Peruvian pyrites gave the same isomer shift of about +0.310 mm sec^{-1} (relative to α-Fe) and a quadrupole splitting of Δ = 0.618 mm sec^{-1}, which agree with literature data for pure stoichiometric pyrite (Vaughan and Craig 1978, Greenwood and Gibb 1971). Electron microprobe analyses, XRD patterns, and Mössbauer spectroscopy on a silicate concentrate show that the major impurity in the Spanish pyrite is chloritoid ($Fe_2Al_4Si_2O_{10}(OH)_4$). XRD patterns of the silicate concentrates from unreacted and reacted pyrite samples showed that the chloritoid does not react under the experimental conditions used in the runs. In fact, kinetic data from the Spanish and Peruvian pyrites are indistinguishable.

The pyrite was cut into slices about 1–2 × 1 cm and 1 mm thickness (see Tables I and II). Samples run at BU were polished to 1 μm and those run at Washington University were polished to 0.25 μm, to ensure a smooth

TABLE I
Pyrite Decomposition Experiments Done at Boston University

Run No.[a]	T (°C)	Time (min)	Length a_o (cm)	Width b_o (cm)	Thickness c_o (cm)	Fractional Mass Loss	α Fraction of pyrite left gravim.[b]	gravim.	log Rate linear eq. log (cm/h)	log Rate cubic eq. log (cm/h)	Phase(s) in Reacted Sample[c]	Gas mixture
Experiments in pure CO_2												
VS-9	464	50	0.474	0.428	0.084	0.0109	0.9524	0.9674 py-hem	-2.785	-2.919	py, hem, mag	
VS-5	516	5	0.557	0.401	0.081	0.0070	0.9695	0.9804 py-hem	-1.994	-2.122	py + hem	
VS-6	524	40	0.553	0.401	0.062	0.0692	0.6979	-	-1.853	-1.930	py + m-Fe_7S_8 + mag? + hem?	
VS-7	577	32	0.473#	0.323#	0.030	0.2457	0	-	>-1.521	> -1.515	po	
VS-10H	598	5	0.708	0.420	0.086	0.0389	0.8302	-	-1.057	-1.165	py + m-Fe_7S_8 + mag + hem	
VS-8	628	5	0.479	0.477	0.087	0.0742	0.6761	-	-0.772	-0.874	py + m-Fe_7S_8	
VS-3	645	15	0.557	0.401	0.077	0.2466	0	-	> -0.781	> -0.765	h-Fe_7S_8 + mag + hem	
VS-4	728	5	0.479	0.477	0.089	0.2277	0.0061	-	-0.275	-0.277	h-Fe_9S_{10}	
VS-2	845	10	0.477	0.474	0.157	0.2672	0	-	>-0.260	> -0.357	m-Fe_7S_8 + mag? +hem	
VS-1	1012	60	0.555	0.399	0.064	-	0	-	-	-	mag *	
CO_2-H_2 gas mixtures												
VS-16H	504	20	0.791	0.447#	0.041	0.0130	0.9434	0.9636 py-hem	-2.622	-2.679	py	70% CO_2, 30% H_2
VS-14H	513	24	0.709	0.434	0.075	0.0130	0.9433	0.9611 py-hem	-2.439	-2.542	py +mag? + hem?	14% CO_2, 86% H_2
VS-15H	507	5	0.705	0.463	0.092	0.0007	0.9970	0.9980 py-hem	-2.945	-3.068	py + mag? + hem	2.5% CO_2, 97.5% H_2
VS-11H	698	5	0.706	0.475	0.082	0.2327	0	-	> -0.300	> -0.297	h-Fe_9S_{10} + hem	76% CO_2, 24% H_2
VS-12H	694	5	0.701	0.39	0.084	0.2476	0	-	> -0.262	> -0.245	h-Fe_7S_8 + mag + hem	58% CO_2, 42% H_2
VS-13H	691	5	0.712	0.374	0.080	0.2489	0	-	> -0.281	> -0.264	??? FeS + h-$Fe_{11}S_{12}$ + mag	49% CO_2, 51% H_2

[a] An (H) indicates that pyrite from Chester, VT from the Harvard mineralogical collection was used. All other runs used pyrite from a felsic schist from an unknown locality from the Boston University mineralogical collection.

[b] Gravimetric calculations assuming that pyrite is converted to Fe_7S_8. The next column lists the fraction of pyrite left assuming conversion to hematite (hem).

[c] The phase assemblage determined by X-ray diffraction (XRD). The most intense compound is underlined. The abbreviations used are py, pyrite; mag, magnetite; hem, hematite; po, pyrrhotite; m, monoclinic; h, hexagonal; ?, probably present; n.a., not analyzed.

Approximate value; sample not perfectly rectangular.

* The run product was a ball of magnetite and magnetite dendrites adhering to Pt wire. It is interpreted as an oxidation product of molten sulfide.

surface. Prior to reaction the sample dimensions were measured with a micrometer to ±0.0025 cm (BU) or to ±0.00025 cm (WU) and were weighed to ±0.1 mg (BU) or to ±0.001 mg (WU). These measurements allowed us to calculate the densities of the samples and therefore provided an additional check for impurities. The average density of the pyrite samples run at BU and WU was about 4.75 g cm^{-3} versus densities of 4.89–5.03 g cm^{-3} tabulated by Deer *et al.* (1963). The densities suggest that the pyrites contain a few percent of inclusions, consistent with optical inspection, the gravimetric data, the INAA data, and chloritoid abundances from Mössbauer spectroscopy.

Experimental Methods

The slices were hung from fine Pt-wire harnesses (BU) or placed in ceramic sample holders which gripped the edges of the samples (WU) and were placed next to or hung from an S- or R-type thermocouple. Samples were inserted under rapidly flowing (500–800 cm^3 min^{-1}, 45 to 60 cm min^{-1}) CO_2 into the isothermal hot zones of Del Tech vertical tube furnaces, which were set to the run temperature. Some initial experiments at WU were conducted by placing the pyrite slices in a corundum crucible which was cut open on the sides to allow better gas circulation, but optical microscopy showed that some of these experiments led to reaction on only one side of the samples. These runs are not used for analysis of the kinetic data.

After the sample was inserted into the furnace, the pyrite came up to the run temperature in 3–6 min and then was reacted at constant temperature and at atmospheric pressure in pure CO_2 (BU and WU) or in CO_2–H_2 (BU), Ar–CO_2 (WU), CO_2–CO (WU), CO_2–SO_2 (WU), or CO_2–CO-SO_2 (WU) mixtures for different time periods. The run temperatures were generally 390 to 530°C, corresponding to altitudes of <0 to 9 km on the surface of Venus. In addition, some reactions at BU were performed up to 1000°C. The estimated total uncertainty in the run temperature is ±3°C. After the desired reaction time the furnace power was reduced, the reactant gas was turned

TABLE II
Pyrite Decomposition Experiments done at Washington University

Run No.[a]	Temp T (°C)	Time T (h)	Length a_o (cm)	Width b_o (cm)	Thickness c_o (cm)	Fractional Mass Loss	α fraction of pyrite left gravimetric [b]py-Fe_7S_8		Mössbauer	Pyrite Thickness end/initial	log Rate[c] linear eq. log (cm/h)	cubic eq. log(cm/h)	Phase(s) in Reacted Sample [d]
Experiments in pure CO_2													
52	391	96	1.4359	1.3802	0.0742	0.0117	0.949	-	n.a.	0.928	-4.705	-4.747	py + m-Fe_7S_8 + mag
54	390	167	1.3713	1.3393	0.0739	0.0130	0.943	0.961 hem	n.a.	0.943	-5.066	-5.109	py + hem
108 P	389	334.5	1.7966	0.9480	0.0609	0.0831	0.637	0.752 hem	n.a.	0.558	-4.646	-4.677	py + hem
37	421	29.5	1.3368	1.3726	0.0742	0.0091	0.960	-	n.a.	0.940	-4.301	-4.344	py + m-Fe_7S_8
36	416	30	1.4277	1.3815	0.0739	0.0064	0.972	-	n.a.	0.932	-4.463	-4.506	py + m-Fe_7S_8
17	413	47	1.2151	1.2438	0.0617	0.0251	0.891	-	n.a.	0.844	-4.143	-4.181	py + m-Fe_7S_8
15	413	48	1.2461	1.2111	0.0638	0.0318	0.861	-	n.a.	0.909	-4.035	-4.073	py + m-Fe_7S_8
12	412	96	1.1748	1.0259	0.0635	0.0290	0.874	-	0.910	0.652	-4.378	-4.421	py + m-Fe_7S_8 + (mag) + (hem)
38	421	140	1.3660	1.3546	0.0744	0.0400	0.826	-	0.857	0.793	-4.333	-4.372	py + m-Fe_7S_8 + (mag) + (hem)
14	413	161	1.2436	1.2136	0.0643	0.0773	0.662	-	0.624	0.705	-4.172	-4.202	py + m-Fe_7S_8 + mag + hem
18	413	233	1.2042	1.2555	0.0602	0.1032	0.550	-	0.602	0.400	-4.235	-4.259	py + m-Fe_7S_8 + (mag) + hem
55	419	235	1.6040	1.2598	0.0747	0.1158	0.495	-	n.a.	0.321	-4.095	-4.118	py + m/h-Fe_7S_8 + mag + hem
56	417	236	1.3479	0.9417	0.0728	0.1538	0.329	0.353 hpo	n.a.	0.554	-4.001	-4.022	py + h-Fe_9S_{10} + mag +hem
58	417	259.7	1.7021	1.3033	0.0747	0.0609	0.734	0.744 hpo	n.a.	0.747	-4.434	-4.466	py + h-Fe_9S_{10} + hem
39	415	454	1.3625	1.4069	0.0744	0.0709	0.691	0.702 hpo	n.a.	0.801	-4.612	-4.644	py + h-Fe_9S_{10}
7	466	4.5	1.1750	1.0201	0.0627	0.0119	0.948	-	n.a.	0.921	-3.442	-3.486	py + m-Fe_7S_8
10	461	15.3	1.2507	1.2083	0.0643	0.0227	0.901	-	n.a.	0.850	-3.682	-3.721	py + m-Fe_7S_8
8	467	24	1.1750	1.1750	0.0648	0.0380	0.834	-	0.833	0.848	-3.650	-3.692	py + m-Fe_7S_8 + (mag) + (hem)
11	468	41	1.4910	1.1867	0.0683	0.0478	0.792	-	0.794	0.786	-3.760	-3.795	py + m-Fe_7S_8 + (mag) + (hem)
27	473	41	1.4790	1.1953	0.1341	0.0202	0.912	-	n.a.	0.861	-3.841	-3.916	py + m-Fe_7S_8
25	470	41	1.4709	1.2035	0.1349	0.0167	0.927	-	n.a.	0.845	-3.921	-3.997	py + m-Fe_7S_8
9	466	65	1.1758	1.0277	0.0635	0.0942	0.589	-	0.594	0.732	-3.697	-3.727	py + m-Fe_7S_8 + (mag) + (hem)
29	473	68	1.4722	1.2062	0.1344	0.0344	0.850	-	n.a.	0.782	-3.829	-3.899	py + m-Fe_7S_8
31	472	70	1.2408	1.0787	0.0622	0.0568	0.752	-	n.a.	0.776	-3.958	-3.992	py + m-Fe_7S_8
24	470	71	1.2365	1.2116	0.0638	0.0399	0.826	-	n.a.	0.913	-4.107	-4.143	py + m-Fe_7S_8
30	474	71	1.4702	1.1567	0.1341	0.0380	0.834	-	n.a.	0.751	-3.805	-3.876	py + m-Fe_7S_8
28	470	91	1.5067	1.4181	0.0668	0.0620	0.729	-	n.a.	0.754	-4.003	-4.031	py + m-Fe_7S_8
26	472	94	1.4702	1.2103	0.1341	0.0410	0.821	-	n.a.	0.776	-3.894	-3.962	py + m/h-Fe_7S_8
35	471	95	1.3584	1.2906	0.0726	0.0525	0.771	-	n.a.	0.797	-4.057	-4.093	py + m/h-Fe_7S_8
32	466	187	1.1671	1.1841	0.0478	0.1529	0.332	-	0.413	0.246	-4.070	-4.082	py + m/h-Fe_7S_8 + (mag) + (hem)

off, a rapid (500–800 cm^3 min^{-1}) CO_2 flow was turned on, and the sample was lifted to the cooled top of the furnace and was allowed to cool below 90°C. The rapid CO_2 flow flushed out the furnace tube once every 1.5–2 min. The time required for cooling was 3–5 min. The kinetic data in Tables I–III show that the short time required for cooling does not lead to any considerable thermal decomposition of pyrite to pyrrhotite.

As shown in Tables I and II, our run products frequently contain monoclinic low-Fe pyrrhotite (Fe_7S_8), which has also been observed by other groups studying pyrite decomposition (e.g., Jagadeesh and Seehra 1981). However, the presence of monoclinic Fe_7S_8 in our run products led a referee to suggest that we needed to quench our samples more rapidly to avoid a phase change from the high-temperature form of low-Fe pyrrhotite, which has a hexagonal crystal structure, to the low-temperature form of low-Fe pyrrhotite, which has a monoclinic crystal structure. In fact, the 1C superstructure, which is the form of hexagonal low-Fe pyrrhotite stable at all our run temperatures (the 1C + pyrite field of the Fe–S phase diagram in Fig. 2b), is unquenchable (Corlett 1968, Kissin and Scott 1982, Kruse 1990, Nakazawa and Morimoto 1970, 1971). The phase boundaries of 1C hexagonal low-Fe pyrrhotite had to be determined by high-temperature X-ray diffraction and other high-temperature methods. The difficulties in doing this led to considerable confusion about the phase boundaries in the Fe–S phase diagram at temperatures below about 350°C (e.g., see the low temperature Fe–S phase diagrams presented by Arnold 1969, Clark 1966, Desborough and Carpenter 1965, Kissin and Scott 1982, Taylor 1970).

The difficulty in quenching hexagonal low-Fe pyrrhotite is indicated by scanning electron microscopy of several of our samples in which X-ray diffraction showed the presence of only monoclinic pyrrhotite. Scanning electron micrographs of these samples revealed hexagonally shaped pyrrhotite crystals. One such example is shown in Fig. 3, which is a micrograph of sample 8. We interpret the observations of hexagonal pyrrhotite crystals in samples having monoclinic pyrrhotite X-ray diffraction patterns as evidence that the hexagonal → monoclinic phase

TABLE II—*Continued*

Run No.[a]	Temp T (°C)	Time T (h)	Length a_o (cm)	Width b_o (cm)	Thickness c_o (cm)	Fractional Mass Loss	α fraction of pyrite left gravimetric [b]py-Fe_7S_8	Mössbauer	Pyrite Thickness end/initial	log Rate[c] linear eq. log (cm/h)	log Rate[c] cubic eq. log(cm/h)	Phase(s) in Reacted Sample [d]
Experiments in pure CO_2												
33	472	329	2.2974	1.6828	0.0744	0.3410	0.341	0.278	0.467	-4.012	-4.027	py + m/h-Fe_7S_8 + (mag) + (hem)
46	501	16	1.4158	1.3795	0.0744	0.0696	0.696	n.a.	0.743	-3.151	-3.183	py + m-Fe_7S_8
48	501	26	1.4257	1.3795	0.0734	0.0879	0.617	n.a.	0.749	-3.266	-3.294	py + m-Fe_7S_8
51	499	43	1.4379	1.3896	0.0744	0.1356	0.408	n.a.	0.654	-3.291	-3.310	py + m/h-Fe_7S_8
50	500	63.1	1.3686	1.3498	0.0732	0.1845	0.195	n.a.	0	-3.331	-3.341	py + m/h-Fe_7S_8
47	530	2.5	1.3726	1.3048	0.0737	0.0357	0.844	0.792	0.801	-2.639	-2.678	py + m-Fe_7S_8 + (mag) + (hem)
44	529	5	1.3780	1.4112	0.0734	0.0729	0.682	0.676	0.704	-2.632	-2.662	py + m-Fe_7S_8 + (mag) + (hem)
49	533	8	1.3485	1.3658	0.0747	0.1078	0.530	0.582	0.463	-2.658	-2.684	py + m-Fe_7S_8 + (hem)
45	532	16	1.4308	1.3815	0.0749	0.2013	0.121	0.011	0.347	-2.687	-2.693	(py) + m-Fe_7S_8 + (mag) + (hem)
42	525	43	1.4445	1.3909	0.0739	0.2321	0	0.005	0	> -3.076	> -3.077	(py) + h-Fe_9S_{10} + (mag) + (hem)
43	533	65	1.4478	1.3894	0.0739	0.2297	0	0.001	0	> -3.260	> -3.262	(py) + h-Fe_9S_{10} + (mag) + (hem)
41	534	97.5	1.3739	1.3472	0.0734	0.2403	0	0.001	0	> -3.419	> -3.490	(py) + h-Fe_9S_{10} + mag + (hem)
40	532	167	1.3680	1.3543	0.0752	0.2517	0	n.a.	0	>-3.623	> -3.620	h-Fe_9S_{10} + mag
0.01 % CO - 99.99 % CO_2												
123 P	390	65.1	0.9759	0.9547	0.0522	0.0063	0.973	0.981 hem	n.a.	0.967	-5.122	-5.166	py + hem
114 P	390	72.8	1.5558	0.9330	0.0525	0.0024	0.990	0.993 hem	n.a.	0.975	-5.595	-5.632	py
117	390	134	1.1080	1.0389	0.0633	0.0259	0.887	0.923 hem	n.a.	0.747	-4.738	-4.783	py + hem
120 P	417	45.3	1.4755	0.9361	0.0516	0.0925	0.596	n.a.	0.788	-3.639	-3.662	py + m-Fe_7S_8
113 P	416	64	1.1298	0.9914	0.0501	0.0924	0.597	n.a.	0.598	-3.793	-3.818	py + m-Fe_7S_8 + hem
115 P	417	72.5	1.0986	0.9576	0.0526	0.1182	0.484	n.a.	0.574	-3.728	-3.749	py + m-Fe_7S_8 + mag? + hem
104 P	471	25	1.7821	0.9454	0.0605	0.0425	0.815	n.a.	0.838	-3.649	-3.682	py + m-Fe_7S_8
122 P	470	64.8	0.9366	0.9600	0.0605	0.2782	0	n.a.	0	> -3.247	> -3.233	py + m/h-Fe_7S_8 + hem
103 P	468	262.5	1.3713	1.2192	0.0605	0.2897	0	n.a.	0	> -3.853	> -3.843	h-Fe_9S_{10} + mag + hem
102 P	468	263	1.3774	1.2174	0.0605	0.2687	0	n.a.	0	> -3.886	> -3.880	h-Fe_9S_{10} + hem
125	500	26.8	1.0839	0.9914	0.0629	0.2399	0	n.a.	0	> -2.910	> -2.907	py + m/h-Fe_7S_8
126	*531*	*5*	*1.3031*	*1.0553*	*0.0632*	*0.1076*	*0.530*	*n.a.*	*0.569*	*-2.527*	*-2.552*	py + m-Fe_7S_8
0.10 % CO - 99.90 % CO_2												
101 P	416	24	1.1082	0.9512	0.0599	0.0331	0.856	0.856	0.896	-3.744	-3.786	py + m-Fe_7S_8 + (mag) + (hem)
100 P	415	24.9	1.3266	1.1994	0.0472	0.0325	0.858	0.855	0.746	-3.871	-3.898	py + m/h-Fe_7S_8 + (mag) + hem
98 P	415	72	1.3688	1.2609	0.0488	0.0913	0.602	0.610	0.591	-3.870	-3.889	py + m/h-Fe_7S_8 + (mag) + hem
99	415	138	1.3708	1.2603	0.0480	0.1618	0.294	0.528	0.458	-3.911	-3.920	py + m/h-Fe_7S_8 + mag? + hem

change for low-Fe pyrrhotite is quite rapid. However, in some cases, we do observe 3C hexagonal low-Fe pyrrhotite in our samples, indicating that they quenched in the NA pyrrhotite + pyrite field of the Fe–S phase diagram in Fig. 2b.

Later, in the results section we discuss the phase composition of our samples and their relationship to the Fe–S phase diagram in some more detail. However, here we want to emphasize two points. First, the Fe–S phase diagram predicts that the composition of the unquenchable 1C hexagonal pyrrhotite (see Fig. 2) ranges from $Fe_{7.14}S_{8.00}$ at 390°C to $Fe_{6.96}S_{8.00}$ at 531°C. Within ±(0.6–2.0)% this composition is the same as that of the monoclinic Fe_7S_8 observed in our samples. Second, we do not see any evidence that the inversion of hexagonal to monoclinic pyrrhotite in some run products alters our kinetic data, because we are concerned with measuring the rate at which pyrite thermally decomposes to pyrrhotite. We are not measuring the rate of the subsequent pyrrhotite phase change nor are we attempting to refine the phase fields in the Fe–S phase diagram. Although more rapid quenching *may* have preserved quenchable superstructures of hexagonal Fe_7S_8 composition in all reacted samples, the fragile product layers would have been damaged and/or lost during quenching into ice water or another low-temperature bath. We decided not to use rapid quenching because a major goal of our work was to preserve the product layers for microscopic examination and for retrieval of kinetic data via thickness measurements.

After cooling, the samples were carefully removed from the sample holder and weighed to determine the mass loss. The samples were then broken to obtain cross-sectional mounts for optical microscopy, scanning electron microscopy (SEM), and electron microprobe work. Other parts were powdered under acetone for XRD and Mössbauer analysis.

Details of Gas Mixing and Oxygen Fugacity Measurements

The CO_2–H_2 gas mixing runs at BU were done using needle valve rotameters. The experiments at WU used

TABLE II—*Continued*

Run No. [a]	Temp T (°C)	Time T (h)	Length a_o (cm)	Width b_o (cm)	Thickness c_o (cm)	Fractional Mass Loss	α fraction of pyrite left gravimetric [b]py-Fe_7S_8		Mössbauer	Pyrite Thickness end/initial	log Rate[c] linear eq. log (cm/h)	cubic eq. log(cm/h)	Phase(s) in Reacted Sample [d]
0.10 % CO - 99.90 % CO_2													
97	468	72	1.3863	1.2570	0.0488	0.1216	0.469	-	0.333	0.744	-3.745	-3.761	py + m-Fe_7S_8 + (mag)
95	468	149.2	1.3683	1.2545	0.0485	0.2138	0.067	0.100 hpo	0.068	0.563	-3.835	-3.838	h-Fe_9S_{10} + (mag) +hem
96	468	220.9	1.3655	1.3269	0.0485	0.2422	0	-	0.002	0	> -3.951	> -3.950	h-Fe_9S_{10} + mag + hem
1.01% CO -98.99% CO_2													
130	390	48	1.379	0.8057	0.0733	0.0101	0.952	-	n.a.	n.a.	-4.437	-4.493	py + m-Fe_7S_8 + mag? + hem
140P	393	72	1.8873	1.7751	0.0577	0.0144	0.937	-	n.a.	0.887	-4.600	-4.625	py + m-Fe_7S_8
137P	393	163	1.8893	1.7721	0.0581	0.0419	0.817	-	n.a.	0.875	-4.487	-4.509	py + m-Fe_7S_8 + hem
141P	420	22.2	1.8907	1.7710	0.0579	0.0117	0.949	-	n.a.	0.944	-4.177	-4.202	py + m-Fe_7S_8
128	415	41	1.5122	1.5171	0.0718	0.0301	0.869	-	n.a.	n.a.	-3.039	-3.975	py + m-Fe_7S_8
139	419	74.4	1.2874	1.0245	0.0577	0.1174	0.488	-	n.a.	0.447	-3.702	-3.723	py + m/h-Fe_7S_8 + mag + hem
138P	418	164	1.2567	1.0469	0.0573	n.a.	n.a.	-	n.a.	0.280	-3.599	-	py + m/h-Fe_7S_8 + mag + hem
142	468	19.1	1.3892	1.4543	0.0577	0.0621	0.729	-	n.a.	0.750	-3.387	-3.412	py + m-Fe_7S_8
144	468	24.3	1.1361	1.0376	0.0640	0.1141	0.502	-	n.a.	0.411	-3.184	-3.210	py + m-Fe_7S_8
129	470	40.8	1.0904	1.0385	0.0622	0.1946	0.150	-	n.a.	0.389	-3.189	-3.198	py + m/h-Fe_7S_8 + mag
145P	503	3.5	1.8934	1.7742	0.0576	0.0239	0.896	-	n.a.	0.953	-3.067	-3.091	py + m-Fe_7S_8
2.5 % CO - 97.5 % CO_2													
59	417	138	1.3813	0.8898	0.0747	0.0915	0.601	0.615 hpo	n.a.	0.753	-4.057	-4.088	py + h-Fe_9S_{10}
996 ppm O_2 -CO_2													
131	419	46.8	1.7486	0.8812	0.0739	0.0472	0.794	0.859 hem	n.a.	0.906	-3.954	-3.999	py + hem
146	468	25.2	1.3899	1.2589	0.0487	0.2378	-	0.289 hem	n.a.	n.a.	-3.163	-3.172	py + h-Fe_9S_{10} + hem
1.1 % SO_2 - 98.9 % CO_2													
34	467	94	1.3675	1.3442	0.0744	0.0217	0.905	-	n.a.	0.942	-4.426	-4.468	py + m-Fe_7S_8 + mag
60	467	256.5	1.2959	0.8839	0.0660	0.0321	0	-	n.a.	0	-	-	hem
1.9 % CO - 1.8 % SO_2 - 96.3 % CO_2													
86	389	96	1.3106	1.1836	0.0681	0.0209	0.909	-	0.901	0.983	-4.490	-4.532	py + m-Fe_7S_8 + (mag) + (hem)
85	391	165	1.3774	1.2512	0.0749	0.0427	0.814	-	0.850	0.874	-4.374	-4.413	py + m-Fe_7S_8 + (mag) + hem
61	417	24.7	1.3030	0.9840	0.0638	0.0158	0.931	-	0.905	0.949	-4.051	-4.095	py + m-Fe_7S_8 + (mag) + (hem)
75	416	68.5	1.3901	1.2692	0.0714	0.0222	0.903	0.934 hem	0.857	0.965	-4.461	-4.503	py + mag + hem
77	416	113.3	1.3866	1.2784	0.0704	0.0165	0.928	0.951 hem	0.885	0.949	-4.815	-4.857	py + mag + hem
64	415	144	1.3002	1.0097	0.0643	0.0677	0.705	0.798 hem	0.781	0.857	-4.345	-4.383	py + mag + hem
66	418	211	1.3792	0.8827	0.0676	0.0784	0.658	0.766 hem	0.824	0.800	-4.426	-4.467	py + (m-Fe_7S_8) + (mag) + hem

premixed CO_2–CO and CO_2–SO_2 gas mixtures (certified standards accurate to ±2% of the concentration of the minor component) and CO_2–CO–SO_2 gas mixtures prepared from Coleman instrument grade (99.99%) CO_2, CP grade (99.5%) CO, and anhydrous grade (99.98%) SO_2 using needle valve rotameters and electronic mass flow controllers (Tylan Corp.). Coleman instrument grade CO_2 was also used in the pure CO_2 runs at WU. The gas flow rates used in the experiments at BU and WU were generally ~2.5–7 cm min^{-1}. However WU runs 27–31 done at about the same temperature but at different flow rates show that the rate data are independent of gas flow rates in the range of ~2.5–30 cm min^{-1}.

We were initially concerned about the possible presence of O_2 impurities in the CO_2 (Fegley and Lodders 1993a), but eliminated this possibility by measuring the oxygen fugacity of CO_2 from our two different gas suppliers at Washington University. The measurements were made using a zirconia-based ceramic oxygen fugacity sensor ($SIRO_2$ C700+ from Ceramic Oxide Fabricators, Ltd.) and a HP digital voltmeter (model 34401A with $>10^{10}$ ohm impedance). A recent review of the use of zirconia oxygen fugacity sensors is given by Huebner (1987). Over a 500° temperature range the measured oxygen fugacity values were equal to those calculated from the self dissociation of CO_2 ($CO_2 = CO + \frac{1}{2} O_2$). There is no evidence for O_2 impurities >1 ppm in the gas. As discussed later, the large number of experimental runs now available and a correction in an error in prior thermodynamic calculations also lead us to reject an earlier suggestion that hematite in some run products formed by reaction with O_2 impurities in the Coleman grade CO_2 (Fegley and Lodders 1993a).

XRD Analysis

Powdered starting materials and run products were mounted on glass slides and the X-ray diffraction patterns were obtained with an Rigaku powder diffractometer at Washington University. The patterns were taken with Cu$K\alpha$ radiation and calibrated with an external silicon

TABLE II—*Continued*

Run No. [a]	Temp T (°C)	Time T (h)	Length a_o (cm)	Width b_o (cm)	Thickness c_o (cm)	Fractional Mass Loss	α fraction of pyrite left gravimetric [b] $py\text{-}Fe_7S_8$	Mössbauer	Pyrite Thickness end/initial	log Rate [c] linear eq. log (cm/h)	cubic eq. log(cm/h)	Phase(s) in Reacted Sample [d]
1.9 % CO - 1.8 % SO_2 - 96.3 % CO_2												
63	466	1.1	1.3848	0.8778	0.0630	0.0027	0.989 -	0.968	1	-3.472	-3.520	py + (m-Fe_7S_8) + (mag) + (hem)
62	467	21	1.2558	0.9779	0.0638	0.0443	0.807 -	0.814	0.742	-3.532	-3.572	py + m-Fe_7S_8 + (mag) + (hem)
94	473	53.2	1.2451	1.3635	0.0493	0.0291	0.873 -	0.922	0.927	-4.230	-4.230	py + m-Fe_7S_8 + mag + hem?
74	467	70	1.3739	1.2553	0.0696	0.0826	0.640 0.753 hem	0.745	0.875	-3.911	-3.911	py + mag + hem
65	468	142.8	1.3020	0.9223	0.0658	0.2205	0.038 0.341 hem	0.107	0.179	-3.818	-3.837	py + h-$Fe_{9}S_{10}$ + mag + hem
92	498	23	1.3805	1.1623	0.0470	0.0974	0.575 -	0.524	0.643	-3.362	-3.381	py + m/h-Fe_7S_8
89	503	67	1.3879	1.2637	0.0721	0.2147	0.063 -	0.202	0	-3.297	-3.300	py + m/h-Fe_7S_8 + mag
88	505	89.5	1.3873	1.2728	0.0719	0.2517	0 -	0.002	0	> -3.355	> -3.350	m-Fe_7S_8 + mag
81	532	2.5	1.3891	1.2751	0.0734	0.0585	0.745 -	0.653	0.869	-2.426	-2.461	py + m-Fe_7S_8
84	534	5	1.3693	1.2581	0.0706	0.1723	0.248 -	0.095	0.331	-2.275	-2.287	py + m-Fe_7S_8 + mag? + hem
83	534	8	1.3868	1.2659	0.0747	0.1991	0.131 -	0.008	0.427	-2.392	-2.399	py? + m/h-Fe_7S_8 + mag + hem?
82	532	17	1.3891	1.2675	0.0721	0.2539	0 -	0.004	0	> -2.629	> -2.623	m/h-Fe_7S_8 + mag + hem
25% Ar - 75% CO_2												
163	419	27.2	1.5461	1.4187	0.0729	0.0483	0.789 -	n.a.	n.a.	-3.713	-3.748	py + m/h-Fe_7S_8
166	420	94	1.5477	1.4133	0.0711	0.1217	0.469 -	n.a.	0.665	-3.861	-3.888	py + m-Fe_7S_8 + hem
162	467	18	1.5499	1.4123	0.0694	0.0474	0.793 -	n.a.	0.697	-3.400	-3.431	py + m-Fe_7S_8
109 P	470	72	1.7666	0.9416	0.0601	0.1052	0.541 -	n.a.	0.578	-3.717	-3.741	py + m-Fe_7S_8 + mag? + hem
160	467	95.6	1.5508	1.4110	0.0728	0.2070	0.096 -	n.a.	~0	-3.463	-3.467	py + m-Fe_7S_8 + h-Fe_9S_{10}
50% Ar - 50% CO_2												
169P	393	46.5	1.9011	1.7669	0.0576	0.0140	0.939 -	n.a.	0.953	-4.585	-4.611	py
165P	395	99.2	1.8908	1.7746	0.0575	0.0382	0.833 -	n.a.	0.866	-4.480	-4.503	py
155P	397	211.5	1.9033	1.7678	0.0582	0.1062	0.536 -	n.a.	0.762	-4.359	-4.378	py + hem
172	393	257.9	1.7464	0.8991	0.0719	0.1171	0.489 -	n.a.	0.651	-4.312	-4.346	py + hem
158P	419	41	1.8958	1.7668	0.0594	0.0173	0.924 -	n.a.	0.902	-4.262	-4.288	py + m-Fe_7S_8
151	419	75.1	1.3726	0.8959	0.0578	0.1183	0.484 -	n.a.	n.a.	-3.702	-3.725	py + m-Fe_7S_8 + hem
150	474	20.8	1.4570	1.3807	0.0582	0.0945	0.588 -	n.a.	0.530	-3.238	-3.259	py + m-Fe_7S_8
153P	473	43.7	1.9029	1.7655	0.0585	0.0534	0.767 -	n.a.	n.a.	-3.806	-3.827	py + m-Fe_7S_8
111 P	470	72	1.3220	0.9594	0.0599	0.1778	0.224 -	n.a.	0.100	-3.543	-3.442	py + m/h-Fe_7S_8 + mag
74.7% Ar - 25.3% CO_2												
173	424	44.5	1.1069	1.0434	0.0632	0.0812	0.757 -	n.a.	n.a.	-3.764	-3.801	py + hem
171	424	67.4	1.3907	0.9117	0.0561	0.1618	0.516 -	n.a.	0.326	-3.696	-3.719	py + m-Fe_7S_8 + hem
170	425	72.75	1.5519	1.4071	0.0704	0.1579	0.528 -	n.a.	0.342	-3.641	-3.663	py + m-Fe_7S_8 + hem
110 P	470	70	1.3220	0.9420	0.0524	0.2801	0 -	n.a.	0	> -3.337	> -3.326	h-Fe_7S_8 + mag + hem

[a] A (P) indicates that pyrite from Peru was used. All other runs used pyrite from Navajun, Spain.

[b] Gravimetric calculations assuming that pyrite is converted to Fe_7S_8. The next column lists the fraction of pyrite left assuming conversion to hexagonal pyrrhotite (hpo) or hematite (hem).

[c] The rate constant from zero-order kinetics $\log k = \log((1 - \alpha)c_o/2t)$. The next column is the rate constant considering all reacting sides using a cubic equation. These calculations are described in the text.

[d] The phase assemblage determined by X-ray diffraction (XRD). The most intense compound is underlined. The abbreviations are py, pyrite; mag, magnetite; hem, hematite; m, monoclinic; h, hexagonal; ?, probably present; n.a., not analyzed. Compounds in parenthesis are identified by Mössbauer spectroscopy only.

standard (NIST). The compositions of hexagonal pyrrhotites in the run products were determined from the position of the (102) reflection according to the equation given by Yund and Hall (1969):

$$\text{At.\%(Fe in pyrrhotite)} = 45.212 + 72.86(d_{102} - 2.0400) + 311.5\,(d_{102} - 2.0400)^2. \quad (1)$$

The characteristic ($40\bar{8}$, 408) doublet diffraction peaks were used for identification of monoclinic Fe_7S_8 (Vaughan and Craig 1978).

Mössbauer Analysis

The Mössbauer spectra of the unreacted pyrite and run products were measured at the Institut für Kernphysik of the Technische Hochschule, Darmstadt, Germany in transmission geometry at room temperature. The experimental setup consists of a loudspeaker-type drive, developed at Darmstadt (Kankeleit 1964), running in constant

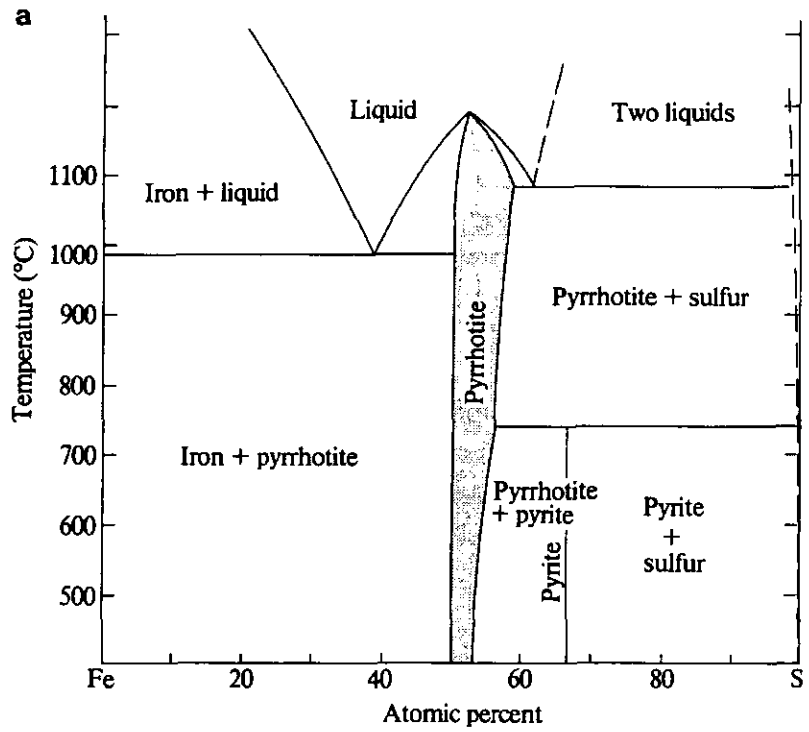
a
Liquid
Two liquids
Iron + liquid
1100
1000
900
800
700
600
500
Temperature (°C)
Pyrrhotite
Pyrrhotite + sulfur
Iron + pyrrhotite
Pyrrhotite + pyrite
Pyrite + sulfur
Pyrite
Fe
20
40
60
80
S
Atomic percent

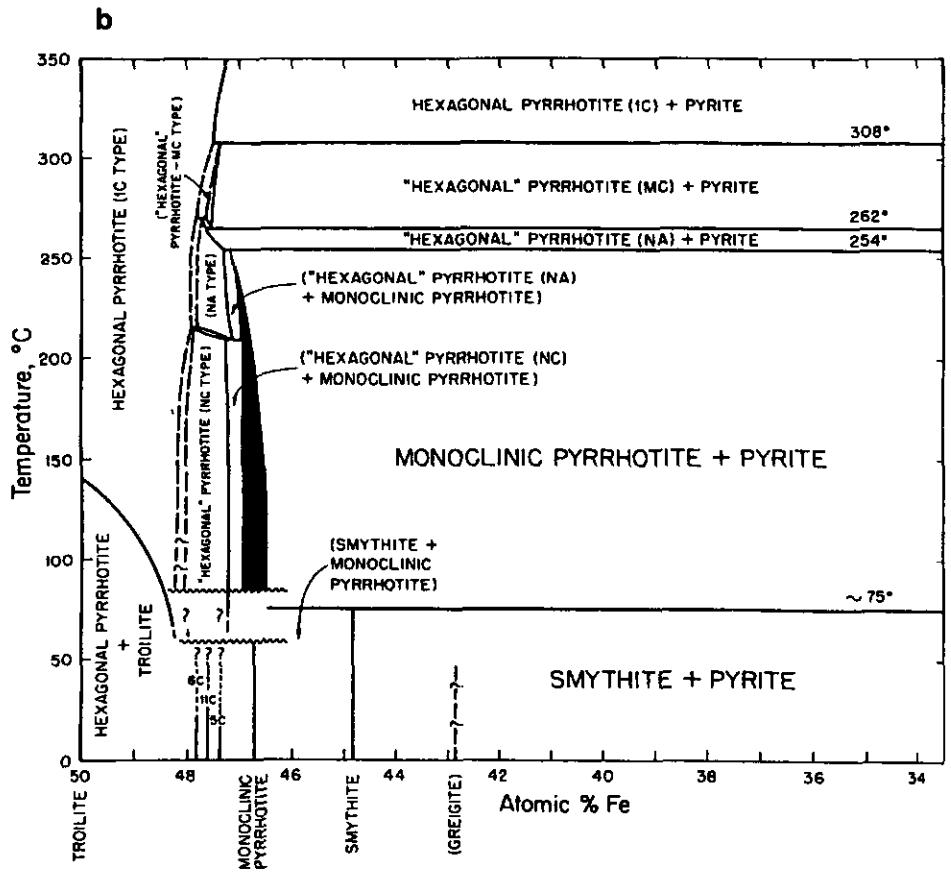
b
HEXAGONAL PYRRHOTITE (1C) + PYRITE
308°
"HEXAGONAL" PYRRHOTITE (MC) + PYRITE
262°
"HEXAGONAL" PYRRHOTITE (NA) + PYRITE
254°
("HEXAGONAL" PYRRHOTITE (NA) + MONOCLINIC PYRRHOTITE)
("HEXAGONAL" PYRRHOTITE (NC) + MONOCLINIC PYRRHOTITE)
MONOCLINIC PYRRHOTITE + PYRITE
(SMYTHITE + MONOCLINIC PYRRHOTITE)
~ 75°
SMYTHITE + PYRITE
HEXAGONAL PYRRHOTITE (1C TYPE)
("HEXAGONAL" PYRRHOTITE - MC TYPE)
"HEXAGONAL" PYRRHOTITE (NA TYPE)
"HEXAGONAL" PYRRHOTITE (NC TYPE)
HEXAGONAL PYRRHOTITE + TROILITE
Temperature, °C
350
300
250
200
150
100
50
0
50
48
46
44
42
40
38
36
34
Atomic % Fe
TROILITE
MONOCLINIC PYRRHOTITE
SMYTHITE
(GREIGITE)

acceleration mode, and a Si PIN diode (Klingelhöfer *et al.* 1992, Held *et al.* 1993; Kankeleit *et al.* 1994) for the detection of the 14.4 keV Mössbauer radiation. ^{57}Co/Rh Mössbauer sources of activities of about 70 and 250 mCi were used, having line widths of about 0.16 and 0.18 mm sec^{-1}, respectively. The typical absorber thickness used for the measurements was about 20 mg cm^{-2}. Thickness effects can be assumed to be small. Recording times for one spectrum are about 2–4 days using the 70-mCi source. The data were fitted using a sum of nine subspectra. This was necessary because the run products contain residual pyrite (one doublet), which in the case of the Spanish pyrite is contaminated by minor amounts of chloritoid (one doublet), and the reaction products pyrrhotite (four sextets), hematite (one sextet), and magnetite (two sextets). The iron oxides are not present in all samples. All isomer shift values in this paper are reported relative to α-Fe.

The relative intensities of the different Fe-bearing phases are given by the area of the subspectra, which are proportional to the relative amounts of the Fe phases and the Debye–Waller factors f (Meisel *et al.* 1990). From this, the weight percentage of each Fe component can be calculated taking into account the stoichiometric factor S,

$$g_k = \frac{A_k \cdot S_K}{\sum_i A_i \cdot S_i \cdot \varepsilon_i^K}, \qquad (2)$$

where g_k is the weight percentage of component K, A_k is the relative area (fraction of total resonant area of the spectrum) of component K, S_k is the stoichiometric factor given by the ratio of the molecular weight of the component and the molecular weight of Fe divided by the number of Fe atoms per molecule, ε_i^K is the ratio of Debye–Waller factors of component K and $i(f_k/f_i)$, and g_k is normalized to the sum of g_i of all components.

The Debye–Waller factors used for these analyses are 0.58, 0.45, 0.64, 0.672, and 0.698 for pyrite, pyrrhotite, hematite, magnetite, and chloritoid, respectively. The f factors for pyrite, pyrrhotite, and hematite are from Fysh

TABLE III
Rate Constants and Pyrite Lifetimes

T (K)	Rate Constant k (cm/hour)	Pyrite Lifetime (days/cm)
	CO_2	
663±1	(1.56±0.69)10^{-5}	2671±1181
689±3	(5.57±1.80)10^{-5}	748±242
742±4	(1.36±0.65)10^{-4}	306±146
773±1	(5.28±0.82)10^{-4}	79±13
804±2	(2.09±0.06)10^{-3}	19.9±0.6
[b] *Activation Energy: 142±17 kJ/mole*		
	50% Ar - 50% CO_2	
668±2	(3.57±1.00)10^{-5}	1167±327
692±1[c]	(9.85)10^{-5}	423
745±2	(3.54±2.38)10^{-4}	118±79
[b] *Activation Energy: 120±15 kJ/mole*		
	100 ppm CO - CO_2	
663±1	(8.55±7.22)10^{-6}	4876±4118
690±1	(1.83±0.33)10^{-4}	288±41
744±1[a]	(2.08)10^{-4}	200
804±1	(2.81)10^{-3}	15
[b] *Activation Energy: 156±45 kJ/mole*		
	1.01% CO - CO_2	
665±2	(2.89±0.50)10^{-5}	1442±250
691±2	(1.19±0.75)10^{-4}	350±221
742±2	(5.46±1.46)10^{-4}	76±20
[b] *Activation Energy: 153±21 kJ/mole*		
	1.9% CO - 1.8% SO_2 - 96.3% CO_2	
663±1	(3.40±0.66)10^{-5}	1225±238
689±2	(4.02±2.46)10^{-5}	1036±634
741±3	(1.79±1.02)10^{-4}	233±133
775±4	(4.59±0.60)10^{-4}	91±12
806±2	(4.21±0.87)10^{-3}	9.9±2
[b] *Activation Energy: 141±27 kJ/mole*		

[a] Only one data point for this isotherm and gas mixture.
[b] Unweighted linear least-square fit.
[c] Mean of two data points.

FIG. 2. The Fe–S phase diagram. (a) Phase relations above 400°C. Reproduced from Vaughan and Craig (1978) and based on the experimental work of Kullerud and Yoder (1959), Toulmin and Barton (1964), and Arnold (1969). Our experiments fall within the pyrrhotite + pyrite and pyrrhotite fields, which are shown in greater detail in the lower diagram. (b) Phase relations below 350°C for the pyrrhotite + pyrite and pyrrhotite fields. Reproduced from Kissin and Scott (1982) and based upon their work and prior studies cited in their paper. The pyrrhotite structures are described in terms of superstructures of the NiAs cell (Morimoto and Nakazawa 1968; Morimoto *et al.* 1975; Nakazawa and Morimoto 1970, 1971). The NA superstructure is also referred to as the 3C superstructure. Our run temperatures of 390–531°C fall within the 1C hexagonal pyrrhotite + pyrite field. However, as noted in the text, previous studies of the Fe–S phase diagram showed that 1C hexagonal pyrrhotite is unquenchable. Instead we find that our run products with low-Fe pyrrhotite (essentially Fe_7S_8), fall within phase fields containing quenchable hexagonal pyrrhotite superstructures and/or 4C monoclinic pyrrhotite. As discussed in the text, the chemical composition of 1C hexagonal pyrrhotite ranges from $Fe_{7.14}S_{8.00}$ at 390°C to $Fe_{6.96}S_{8.00}$ at 531°C. Within ±(0.6–2.0)% this composition is the same as that of the monoclinic Fe_7S_8 observed in our reacted samples.

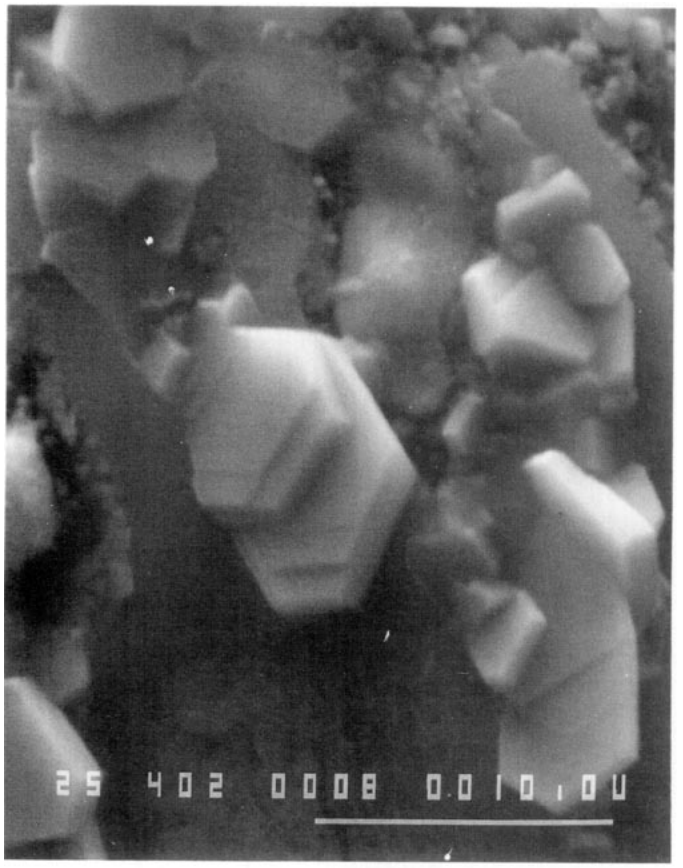

FIG. 3. A scanning electron micrograph of pyrrhotite crystals growing on the surface of sample 8. The crystals have a hexagonal shape although the X-ray diffraction data and Mössbauer spectra show monoclinic pyrrhotite in the run product. As discussed in the text, hexagonal pyrrhotite rapidly reverts to the low-temperature monoclinic structure upon cooling. Scale bar = 10 microns.

(1986); for magnetite and chloritoid the values relative to hematite were taken from DeGrave and Alboom (1991). It is important to note that determination of the weight percentage of the different Fe-bearing phases requires only that the relative f factors be known with sufficient accuracy.

EXPERIMENTAL RESULTS AND REACTION SCHEME

General Observations

The experimental data are summarized in Tables I (BU runs) and II (WU runs). For a better overview, the data in the tables are sorted by different gas mixtures used, temperature, and increasing reaction time. Based on these data and the Fe–S phase diagram in Fig. 2, we propose the following reaction scheme: (a) pyrite thermal decomposition and sulfur loss to form low-Fe pyrrhotite with the approximate composition Fe_7S_8, (b) growth of low-Fe pyrrhotite at the expense of pyrite leading eventually to complete decomposition of all pyrite, (c) thermal decomposition and sulfur loss from the low-Fe pyrrhotite leading to production of more Fe-rich pyrrhotite closer in composition to FeS, (d) oxidation of pyrrhotite to form magnetite, and (e) oxidation of magnetite to maghemite and hematite. Although this scheme is presented as a series of sequential steps, the mixture of phases observed in different run products shows that there is some overlap between all steps. Each step of this proposed scheme is discussed in more detail below, beginning with the initial formation of low-Fe pyrrhotite. The data in Table II form the basis for most of this discussion because of the larger number of runs done and the more extensive characterization of the run products.

Finally, before proceeding, we also emphasize that although we use the Fe–S phase diagram to interpret assemblages observed in the reacted samples, the run products are nonequilibrium assemblages with compositions and mineralogies mainly controlled by kinetics. The run products were not formed at equilibrium in sealed tubes under the equilibrium sulfur vapor pressure, which were the conditions used to determine the phase diagram. This was not done because, as discussed in the Introduction, the sulfur fugacity in the lower atmosphere of Venus is below the level needed to stabilize pyrite (e.g., Fegley and Treiman 1992). Sealed tube experiments are irrelevant to the kinetics of atmosphere–surface reactions on Venus, because these reactions are proceeding in an open, dynamic system.

Step (a): Formation of low-Fe pyrrhotite. With a few exceptions, the results of heating pyrite in pure CO_2 and CO_2 gas mixtures for short time periods were run products dominantly composed of pyrite with smaller amounts of monoclinic Fe_7S_8 (e.g., see the shortest time runs for each gas composition in Table II). The few exceptions, which are runs done at about 390°C in CO_2 mixtures containing either 0.01% CO or 50% Ar, gave pyrite + hematite assemblages. These runs are discussed later in connection with step (d), pyrrhotite oxidation.

As noted earlier, the 1C superstructure of hexagonal low-Fe pyrrhotite is stable at all of our run temperatures, but is unquenchable. X-ray diffraction showed 4C monoclinic Fe_7S_8 in about 75% of all Fe_7S_8-bearing run products, due to the inversion of the higher temperature hexagonal pyrrhotite during the 3–5 min quench period. We used an enlarged version of the Fe–S phase diagram in Fig. 2 to calculate the hexagonal pyrrhotite compositions for the five temperatures at which experiments were conducted. As discussed earlier, the predicted pyrrhotite composition ranges from $Fe_{7.14}S_{8.00}$ at 390°C, the lowest temperature studied, to $Fe_{6.96}S_{8.00}$ at 531°C, the highest temperature studied. This is a change of about ±(0.6 –

2.0)% relative to the formula Fe_7S_8. Thus, the monoclinic pyrrhotite, which is observed in the run products, has essentially the same chemical composition as the hexagonal pyrrhotite stable at our run temperatures.

The experiments done in pure CO_2 also gave elemental sulfur condensation in the water-cooled gas outlet fitting at the top of the furnace, consistent with the net thermochemical reaction

$$7FeS_2 = Fe_7S_8 + 3S_2(g). \quad (3)$$

Precipitation of elemental sulfur was not observed in CO-bearing gas mixtures. The formation of COS via the net thermochemical gas phase reaction

$$S_2(g) + 2CO(g) = 2COS(g) \quad (4)$$

plausibly consumes gas phase sulfur and prevents it from precipitating.

Step (b): Growth of low-Fe pyrrhotite. With increasing time along an isotherm, the amount of pyrite in the run products decreases and the amount of pyrrhotite increases. These changes are a consequence of the loss of sulfur from the experimental charges. The photographs in Fig. 4 show the pyrrhotite layer growing at the expense of the pyrite core in three different run products. From top to bottom, the samples were heated in CO_2 for 2.5, 8, and 167 hr at 530 ± 5°C (runs 47, 49, 40). The Fe_7S_8 layer is about 0.12 mm thick after 2.5 hr and is about 0.35 mm thick after 8 hr. The data in Table II for the fraction of pyrite left as a function of time show the same trend, expressed in terms of the fractional amount of the original pyrite which is present after heating for a given time.

Step (c): Production of high-Fe pyrrhotite. With increasing time of heating along an isotherm, pyrite becomes less abundant than pyrrhotite and a gradual conversion from monoclinic Fe_7S_8 to hexagonal Fe_7S_8 is observed in the run products (Table II and Fig. 5). The hexagonal Fe_7S_8 observed in some run products (e.g., 26, 32, 35, 50, 51, 55, 122, 125) is possibly due to preservation of hexagonal pyrrhotite (in the NA pyrrhotite + pyrite fields of Fig. 2) during quenching because the X-ray patterns match 3C (also known as NA) hexagonal Fe_7S_8. In some of these cases (e.g., runs 50, 51, 122, 125), sulfur loss during pyrite decomposition has moved the bulk Fe/S ratio in the run products to larger values, and pyrrhotite, instead of pyrite, is the major phase in the reacted samples. An alternative explanation for the presence of hexagonal and monoclinic pyrrhotite in these samples is that they quenched in the NC + monoclinic pyrrhotite field of Fig. 2. In this case the smaller amounts of pyrite left in the run products would be nonequilibrium remnants.

Hexagonal Fe_9S_{10} is observed in several run products (e.g., 39–43, 58) that were either heated for fairly long times (10–19 days) or at the highest temperature studied, ~530°C. Fe_9S_{10} is known as 5C pyrrhotite and is a discrete, naturally occurring phase (e.g., Morimoto *et al.* 1975). The Fe_9S_{10}-bearing samples have even larger bulk Fe/S ratios than the hexagonal Fe_7S_8-bearing samples and plausibly quenched into the NC hexagonal pyrrhotite field of Fig. 2. However, the presence of pyrite in several Fe_9S_{10}-bearing samples (e.g., runs 39, 58) demonstrates that they are nonequilibrium assemblages because there is no stable phase field containing both pyrite and NC pyrrhotite in the Fe–S phase diagram. The conversion from Fe_7S_8 to hexagonal Fe_9S_{10} was monitored by the shift of the pyrrhotite ($40\bar{8}$, 408) to (102) reflection (Yund and Hall 1969). The characteristic doublet for monoclinic Fe_7S_8 became a wide singlet peak and the *d*-spacing shifts to higher values according to the presence of hexagonal pyrrhotites.

The conversion of Fe_7S_8 to hexagonal Fe_9S_{10} is also clearly observed by Mössbauer spectroscopy. As shown in Fig. 6, the shape of the spectrum changes significantly when this conversion occurs (compare R45 and R42 in Fig. 6). Additionally a conversion from Fe-poor to Fe-rich hexagonal pyrrhotite was seen as a function of heating time. The values of the hyperfine fields of the subspectra and their relative intensities change with the Fe content of the pyrrhotite (Kruse 1990).

The fastest conversions from Fe_7S_8 to hexagonal pyrrhotite in the run products were observed in pure CO_2 at 530°C. After pyrite has (almost) completely reacted, the hexagonal Fe_7S_8 releases more sulfur to become Fe_9S_{10}, according to the net reaction

$$9h\text{-}Fe_7S_8 = 7h\text{-}Fe_9S_{10} + S_2(g). \quad (5)$$

Such a reaction took place in the sample which is shown at the bottom of Fig. 4, where no pyrite is left and the remaining pyrrhotite is hexagonal Fe_9S_{10}.

Step (d): Pyrrhotite oxidation to magnetite. Microscopic studies of many samples (e.g., Fig. 4c) show that the pyrrhotite layers on the run products are rimmed by magnetite. The X-ray diffraction data and Mössbauer spectra also show the presence of magnetite in many samples, with Mössbauer spectroscopy being sensitive to smaller amounts than X-ray diffraction. Mössbauer spectroscopy shows that the magnetite is generally stoichiometric Fe_3O_4 with the expected intensity ratio of the two iron sites of 2 : 1. Both Fe_7S_8 and Fe_9S_{10} are rimmed by magnetite, which generally, although not exclusively, forms in samples heated for longer times and/or at higher

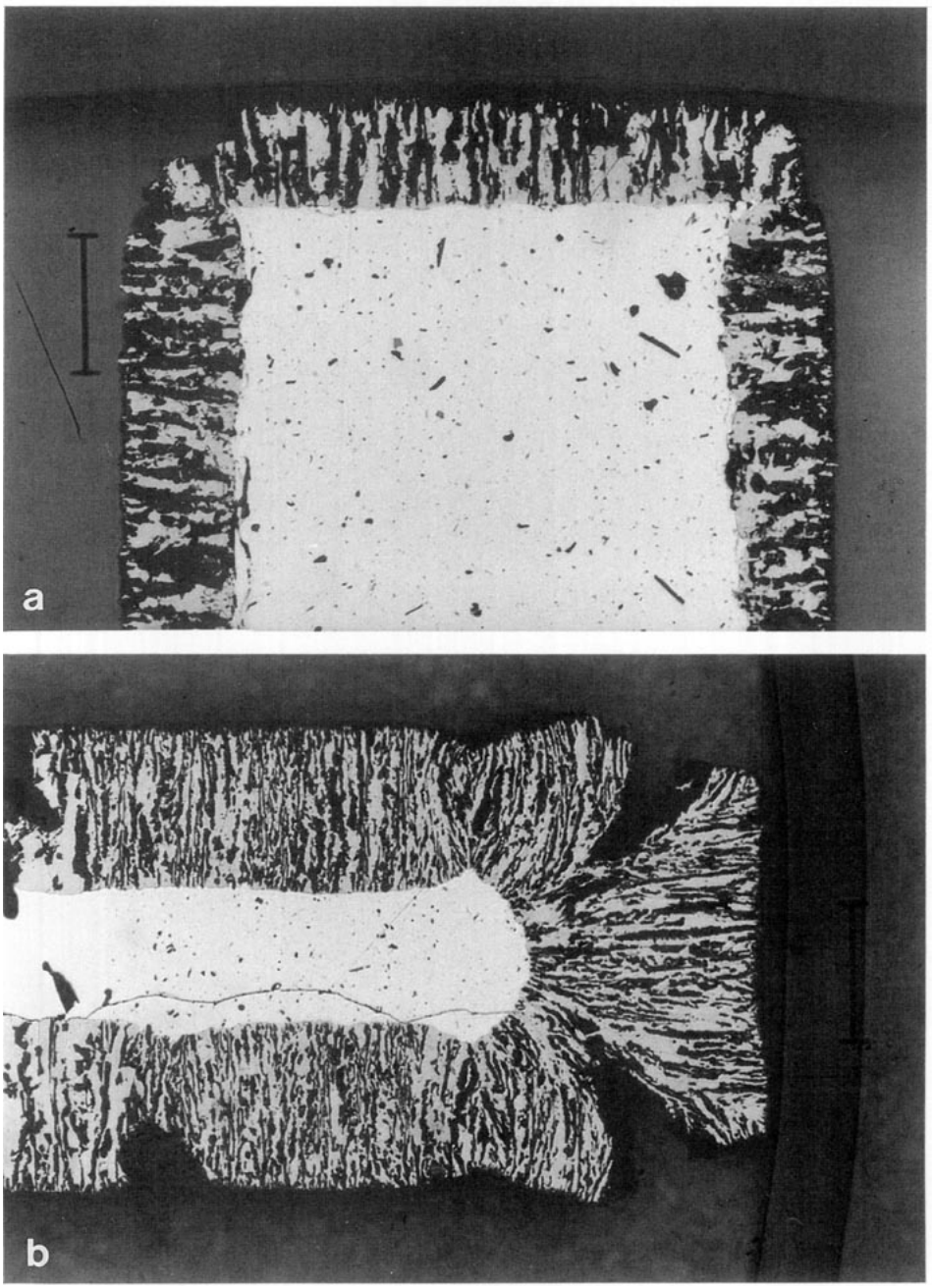

FIG. 4. Reaction progress for samples heated on the 530°C isotherm is illustrated by the increasing thickness of the pyrrhotite layer growing on pyrite. (a) and (b) Fe_7S_8 growing on pyrite. Sample (a) was heated for 2.5 hr and sample (b) for 8 hr. (c) Hexagonal Fe_9S_{10} with no pyrite remaining. This sample was heated for 167 hr. A magnetite layer is growing on the pyrrhotite. Continued sulfur loss drives hexagonal Fe_7S_8 toward increasingly Fe-rich hexagonal pyrrhotite compositions. Pyrrhotite oxidation is a competing reaction which proceeds slower than sulfur loss from pyrrhotite at this temperature. The scale bar = 0.145 mm in (a) and 0.29 mm in (b) and (c).

temperatures. These observations indicate that net thermochemical reactions exemplified by

$$3Fe_7S_8 + 28CO_2 = 7Fe_3O_4 + 12S_2 + 28CO \quad (6)$$

$$Fe_9S_{10} + 12CO_2 = 3Fe_3O_4 + 5S_2 + 12CO \quad (7)$$

have taken place in the run products.

Step (e): Magnetite oxidation to maghemite and hematite. Optical microscopy, X-ray diffraction, and Mössbauer spectroscopy also show that hematite is present in many run products. Generally, hematite is a minor phase found in magnetite-bearing samples and is only detectable by microscopy and Mössbauer spectroscopy (e.g., all samples having (hem) in Table II). However, in several

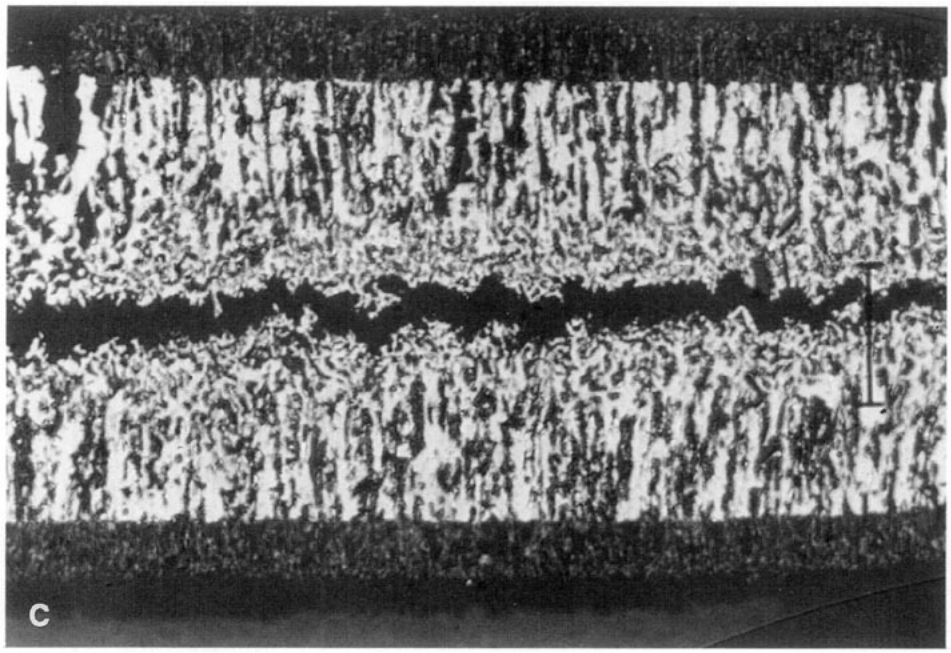

FIG. 4—*Continued*

cases hematite occurs without magnetite and is abundant enough to also be detected by X-ray diffraction. Optical microscopy shows that magnetite is often coated with a thin (<10 μm) bluish gray layer of maghemite (γ-Fe_2O_3), which is surrounded by bright red hematite (α-Fe_2O_3). These observations lead us to propose that maghemite and hematite form by the net thermochemical reactions

$$2Fe_3O_4 + CO_2 = 3\gamma\text{-}Fe_2O_3 + CO \quad (8)$$

$$\gamma\text{-}Fe_2O_3 = \alpha\text{-}Fe_2O_3. \quad (9)$$

Our observations and proposed reactions agree with several prior studies which show that maghemite is thermodynamically metastable with respect to hematite (e.g., Bando *et al.* 1965, Colombo *et al.* 1965, David and Welch 1956, Davis *et al.* 1968, Elder 1965, Feitknecht and Gallagher 1970, Feitknecht and Mannweiler 1967, Gallagher *et al.* 1968, Johnson and Jensen 1974, Kachi *et al.* 1963, Özdemir and Banerjee 1984, Özdemir and Dunlop 1989, O'Neill 1988). However, these studies disagree on the transition temperature at which maghemite changes irreversibly to hematite, with published transition temperatures ranging from about 250 to 900°C. As noted by Özdemir and Banerjee (1984), factors such as the presence of impurities, the method used to prepare the magnetite starting material, and the previous history of the magnetite influence the observed maghemite transition temperature. Our observations of maghemite rimmed by hematite in most of our samples suggests a transition temperature of 390°C. Despite careful examination, the amounts of maghemite in the run products are too small to be detected by XRD or Mössbauer spectroscopy and are only seen by optical microscopy.

At 530°C run products which still contain pyrite never contain larger amounts of magnetite and hematite, indicating that the pyrrhotite to Fe-oxide conversion is much

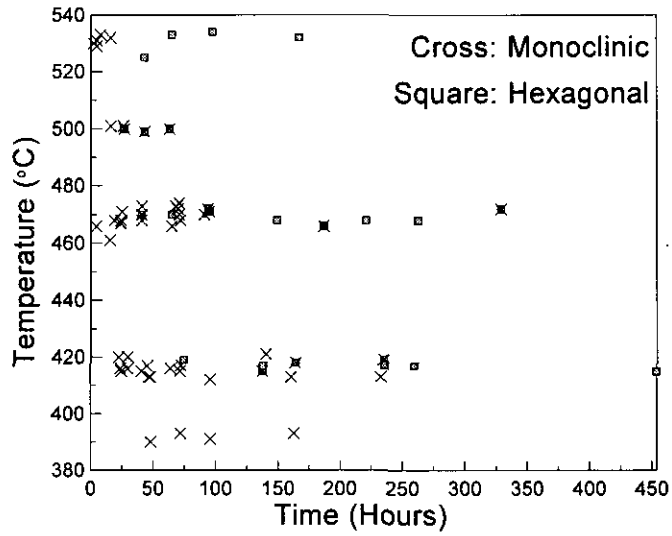

FIG. 5. A plot showing the trend from monoclinic to hexagonal pyrrhotites in the run products with increasing time along an isotherm. X-ray diffraction data summarized in Table II were used to produce the plot.

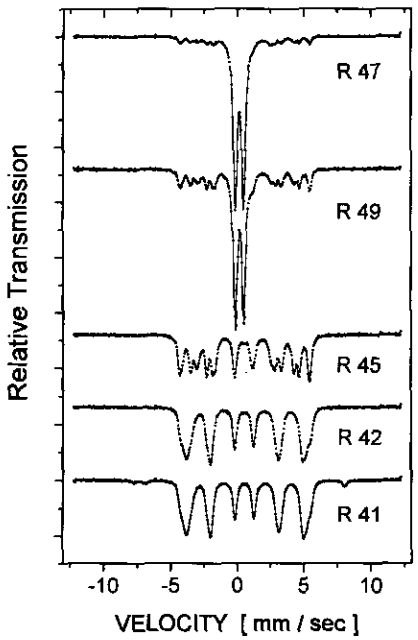

FIG. 6. A set of Mössbauer spectra showing the reaction progress for samples heated on the 530°C isotherm. Going from top to bottom, the samples were heated for 2.5, 8, 16, 43, and 97.5 hr. The first two samples are illustrated in Figs. 4a and 4b. The morphological changes and the changes in the XRD patterns that occur with increasing sulfur loss from pyrite to Fe_7S_8 to more Fe-rich hexagonal pyrrhotite are also visible in the Mössbauer spectra.

slower than the pyrite–pyrrhotite conversion. In contrast, at 390°C, the lowest temperature investigated, no pyrrhotite was found in the products which reacted for the longest times but pyrite and hematite were found instead (e.g., runs 52, 54, 108). This indicates that oxidation of Fe_7S_8 takes place before pyrite fully decomposes and that the oxidation of pyrrhotite is faster than pyrite decomposition at this temperature. This trend is consistent with log k vs $1/T$ plots for the pyrrhotite oxidation and pyrite thermal decomposition rate constants if the activation energy for pyrrhotite oxidation is less than the activation energy for pyrite thermal decomposition. Treiman and Fegley (1991) reported an activation energy of ~18 kJ mole^{-1} for pyrrhotite oxidation, which is less than our derived activation energy of ~150 kJ mole^{-1} for the pyrite to pyrrhotite conversion.

We were initially surprised by the formation of maghemite and hematite in CO–CO_2 gas mixtures because thermodynamic calculations predict that the CO-bearing gas mixtures used in our experiments are in the magnetite stability field (e.g., see Fegley and Treiman 1992). However, we verified that magnetite is converted to hematite in these CO-bearing gas mixtures by performing several additional experiments.

In one set of experiments we heated synthetic magnetite powder in several of the same CO-bearing gas mixtures listed in Table II. The magnetite turned red, and XRD patterns showed only hematite or hematite plus minor magnetite. In a related set of experiments done in the same gas mixtures, we heated CuO, which converted to metallic Cu, thus showing that the gas mixtures were below the CuO–Cu buffer but above the Fe_3O_4–Fe_2O_3 buffer (Fegley *et al.* 1994b). We also studied the oxidation of basalt in CO–CO_2 gas mixtures and showed by Mössbauer spectroscopy that hematite formed during the experiment and that Fe^{3+}-bearing pyroxene increased at the expense of Fe^{2+}- bearing phases (Fegley *et al.* 1994a, b). The observations of magnetite oxidation to hematite and of basalt oxidation to hematite in CO–CO_2 gas mixtures inside the magnetite stability field are consistent with the deductions by Pieters *et al.* (1986) that Fe^{3+} minerals such as hematite are present on the surface of Venus.

Kinetic Treatment

For the kinetic treatment we need to know the fraction of pyrite left (α) in the run products. The α values can be determined in several independent ways. In addition to Mössbauer spectroscopy, which can directly measure the amount of pyrite left in the samples, we can calculate the fraction of pyrite left gravimetrically from the mass loss. Because Fe_7S_8 is the major product in these experiments, we can calculate the fraction of pyrite left (α) as

$$\alpha = 1 - \frac{\Delta W}{W_{\text{ini}}} f_{\text{St}}, \tag{10}$$

where ΔW stands for the mass loss, W_{ini} for initial mass, and $f_{\text{St}} = 4.3649$ is a factor derived from the mass balance of Eq. (3). We show later that the α values determined gravimetrically agree well with the independent α values from Mössbauer spectroscopy (e.g., Table II). The gravimetric data cannot take into account the amount of Fe-oxides formed, but XRD data indicate that Fe-oxides are not detectable or are negligible by-products in most runs, where pyrrhotite is the major reaction product, depending on the duration and temperature. Mössbauer spectroscopy also showed that samples where Fe-oxides were not detected by XRD contain amounts of oxides below 1%. For samples where pyrite was identified in the run products by XRD or optical microscopy and where Fe_7S_8 was absent, the factor in Eq. (10) was changed appropriately for the pyrite to magnetite or hematite conversion, depending on identification of the major phases by XRD. Samples where pyrite was not detected by XRD or by optical microscopy were not included in the kinetic calculations.

The third independent way to monitor the reaction progress was to measure the thickness of the remaining pyrite

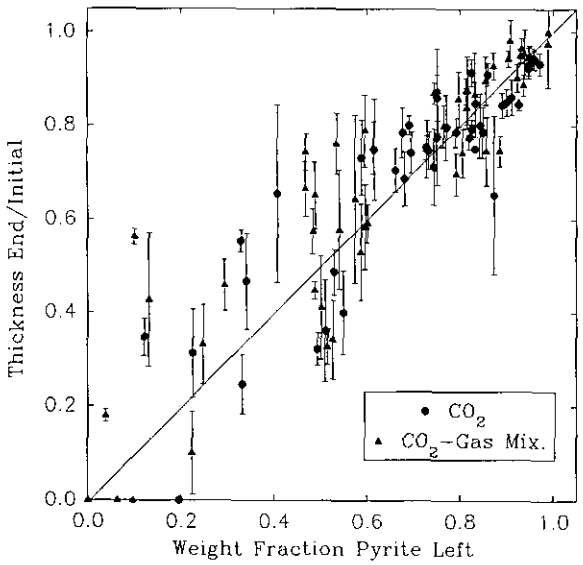

FIG. 7. A plot of the weight fraction of pyrite versus the ratio of final/initial pyrite thickness in the samples. The 1σ error bars on the thickness values are from multiple measurements along the length of a sample. The 1σ errors on the gravimetric data are comparable to the symbol size. The line is a 1 : 1 diagonal shown for comparison.

in the cross-sections of the samples. The ratios of final/initial thickness are also listed in Table II. These ratios were obtained by measuring several segments along the length of the cross-section, taking the mean and computing the 1σ errors. Of all methods chosen to monitor the reaction progress, this method has the highest associated errors. First, the cross sections investigated are only part of the total reacted slice and the layer thickness may be different along the length of the slice. Second, the brittleness of pyrite and the product layers sometimes makes it difficult to obtain good sample splits for mounting.

Rate Law

The kinetics of the pyrite to pyrrhotite conversion were determined from the fraction of unreacted pyrite (α) left in the run products. The α values from experiments at Washington University were fitted to the empirical equation (Brown *et al.* 1980).

$$\ln[-\ln(\alpha)] = m \cdot \ln t + \text{const}, \tag{11}$$

where t is the reaction time. In this equation, values of $m \sim 0.5$ indicate diffusion limited reaction while values of $m \sim 1$ indicate contracting interface kinetics. For all isotherms and gas mixtures, we obtain m values around 1, indicating that contracting interface kinetics are applicable to the pyrite–pyrrhotite reaction, in agreement with prior studies of pyrite decomposition in inert gases or vacuum (Hoare *et al.* 1988, Zhukovskii *et al.* 1967, Samal 1966, Coats and Bright 1966, Pannetier and Davignon 1961). In addition, optical and scanning electron microscopy shows that the pyrrhotite layer is porous and not fully dense so that sulfur can be easily released and escape (e.g., see Fig. 4).

The rate constant (k) is calculated from the α data by considering the geometry of the experimental samples. They are thin rectangular or square plates with initial dimensions a_o, b_o, and c_o. All sides become constantly diminished by $-2kt$ as the reaction proceeds with time (t) and the remaining volume (V) becomes smaller. Because the fraction of pyrite left (α) is proportional to the remaining volume, we can write

$$\alpha = \frac{\text{Vol}_{\text{end}}}{\text{Vol}_o} = \frac{(a_o - 2kt)}{a_o}\frac{(b_o - 2kt)}{b_o}\frac{(c_o - 2kt)}{c_o}, \tag{12}$$

which describes the relationship between the rate constant k, reaction time t, and α (Brown *et al.* 1980). Note that for $a = b = c$ Eq. (12) becomes the well-known contracting volume equation [$\alpha^{1/3} = 1 - kt$].

Because our samples have different a, b, and c dimensions, the calculation of the rate constants for the different isotherms is more complex. However, our samples are thin slices with length (a) and width (b) $\gg$ thickness (c), with c being at most 10% of either a or b. Thus, the decrease of the length a and width b during the reaction is very small ($a \gg kt$, $b \gg kt$) so that $(a_o - 2kt)/a_o \sim (b_o - 2kt)/b_o \approx 1$ and Eq. (12) can be simplified to

$$\alpha = \frac{(c_o - 2kt)}{c_o} = 1 - \frac{2k}{c_o}t, \tag{13}$$

implying zero-order kinetics (constant growth with time). Figure 7, which is a plot of α values versus the measured final/initial thickness ratio for pyrite in the samples, shows that $\alpha = c/c_o$ within the uncertainties of the thickness measurements. An unweighted linear least-squares fit to all the data gives the equation ($\pm 1\sigma$ errors):$c/c_o = 0.09(\pm 0.03) + 0.89(\pm 0.04)\alpha$ (101 samples) for the pyrite thickness ratio. The zero-order rate constants calculated from Eq. (13) are listed in Tables I and II.

Although Fig. 7 shows that the geometry of the samples justifies the approximations involved in deriving Eq. (13), we also solved Eq. (12) considering the actual three-dimensional pyrrhotite layer growth. This was done by substituting $L_o = a_o + b_o + c_o$, $A_o = 2(a_o b_o + a_o c_o + b_o c_o)$, $V_o = a_o b_o c_o$, and transforming Eq. (12) into the cubic equation

$$k^3 - \frac{L_o}{2t}k^2 + \frac{A_o}{8t^2}k + \frac{(\alpha - 1)V_o}{8t^3} = 0. \tag{14}$$

The results for the rate constant from solving Eq. (14) for every run are also given in Tables I and II. The rates determined from the zero-order kinetics (Eq. 13) are up to about 10% larger than the rate constants obtained from Eq. (14) considering all reacting sides. This 10% difference may not be surprising if we keep in mind that the maximum thickness of some samples is also about 10% of length or width.

The agreement between the gravimetric α values and those from Mössbauer spectroscopy is illustrated in Fig. 8. An unweighted linear least-squares fit to all the data gives the equation $\alpha(\text{MB}) = 0.008 + 0.994\alpha(\text{wt.\%})$ with $r^2 = 0.98$ (42 samples). Thus, there is good agreement between the two independent data sets.

In principle, each data set (gravimetric, thickness, and Mössbauer) could be used to calculate pyrite decomposition rate constants. In practice the α values determined gravimetrically from the runs at Washington University were those used. This was done because high-quality gravimetric data are available for all samples and because the Mössbauer spectra were run on splits of the samples instead of the complete samples. This also allows us to compare the two sets of results obtained at BU and Washington University. The rate constants k were calculated from Eq. (13) and (14) and the results are displayed in Fig. 9 and listed (with 1σ uncertainties) in Table III. Also shown in Table III are the activation energies calculated from unweighted linear least-squares fits of the rate constant data and the pyrite lifetimes on the surface of Venus expressed as the number of days to decompose 1 cm of pyrite. These lifetimes are independent of the size of the pyrite deposits.

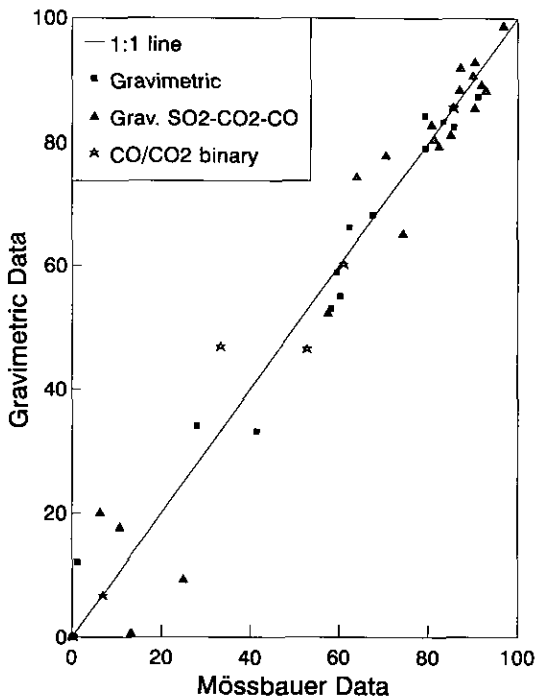

FIG. 8. α values from Mössbauer spectroscopy are compared to those determined from gavimetric data. The 1 : 1 diagonal is for comparison. The 1σ errors on the data are comparable to the point size. The scatter is plausibly due to using small splits of the run products for the Mössbauer spectra.

The laboratory data were obtained at ~1 atm pressure while the surface of Venus is at ~95 atm pressure. Also, the CO and SO_2 mixing ratios at the surface of Venus are lower than those in the laboratory runs. However, experiments done at different CO_2 number densities at ~1 atm pressure show no systematic variation in the pyrite decomposition rate when the CO_2 number density is varied over a factor of 40 (i.e., as the CO_2 concentration was changed from ~100% in pure CO_2, to 75–25% in Ar–CO_2 mixtures, to 70–2.5% in H_2–CO_2 mixtures). The rate data from these experiments are shown in Fig. 10. These data do not provide evidence that the pyrite decomposition rate will be affected by the ~95 times higher CO_2 number density on Venus. The effects of the CO number densities on the pyrite decomposition rate were studied in a series of experiments run in 100 and 1000 ppm and 1.01 and 2.5% CO gas mixtures with CO_2 (e.g., Table II). These experiments showed no systematic variation of the pyrite decomposition rate with the CO number density. It was also possible to calculate activation energies for two sets of CO–CO_2 gas mixture runs. As shown in Table III and in Fig. 11, these activation energies are the same within the 1σ uncertainties as the activation energy in pure CO_2. An extensive set of runs was also made in a CO_2–CO–SO_2 gas mixture with a CO number density ~10 times higher than at the surface of Venus and a SO_2 number density approximately equal to that at the surface of Venus. These runs give rate constants, activation energies, and pyrite lifetimes that are the same within the 1σ uncertainties as those obtained in the pure CO_2 runs. Thus, the experimental data are directly applicable to the surface of Venus.

PROPOSED PYRITE DECOMPOSITION MECHANISM AND APPLICATIONS TO VENUS

The apparent independence of the rate constants and the activation energy on the gas composition indicates that CO_2, CO, and SO_2 are not involved in the rate-determining step for pyrite decomposition and have no role in the formation of the activated complex. The proposed mechanism of S_2 release from pyrite is schematically illustrated in Fig. 12. The derived activation energy of ~150 kJ mole^{-1} is about $\frac{1}{2}$ of the ΔH for pyrite decomposition to pyrrhotite + sulfur vapor over the range 500–552°C (Bog and Rosenqvist 1959). Schwab and Philinis (1947) reported a similar activation energy of 121–138 kJ mole^{-1} for pyrite decomposition at 600–650°C in CO_2. Samal

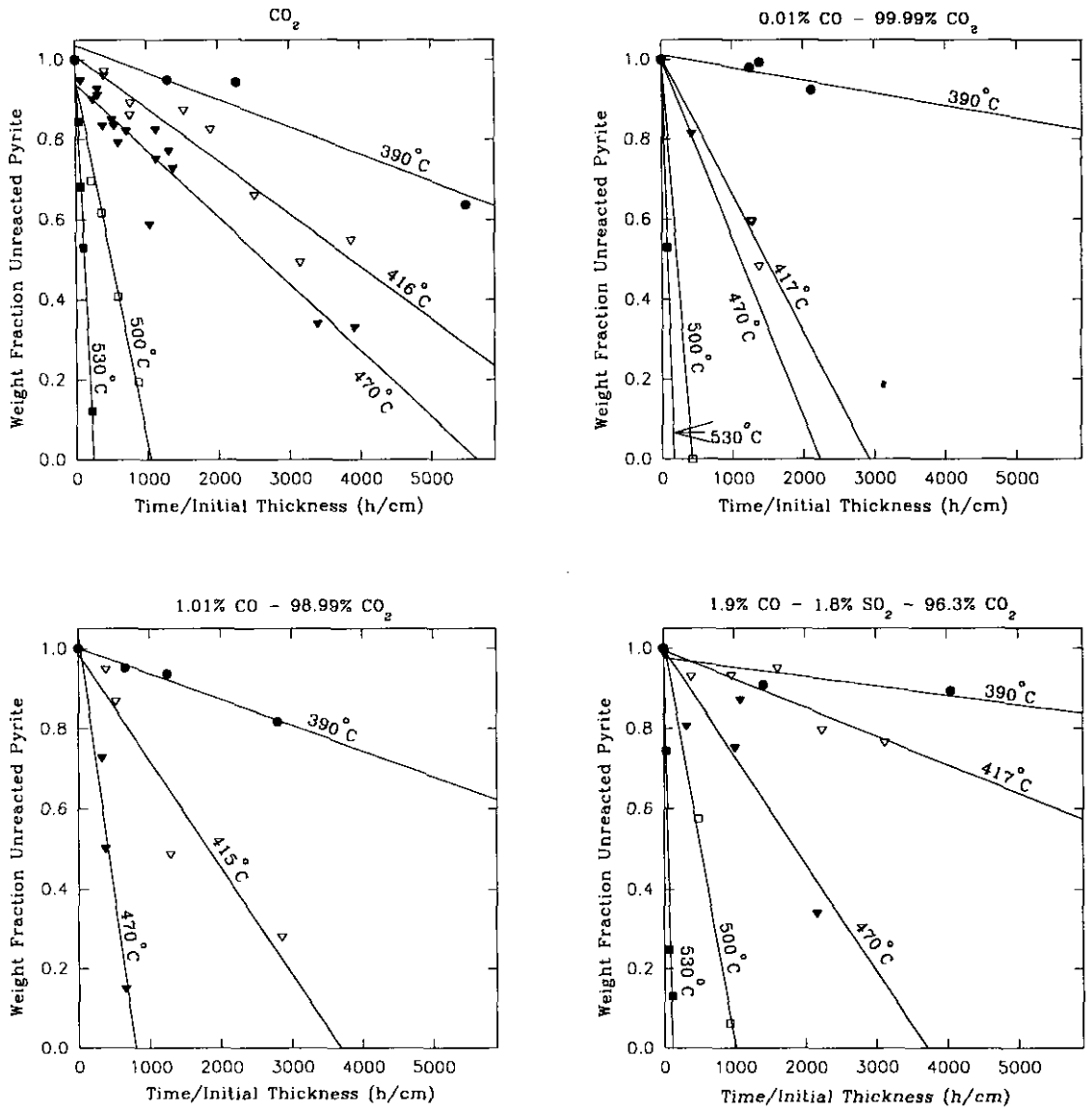

FIG. 9. Pyrite decomposition kinetics in CO_2 and several CO_2 gas mixtures. These graphs illustrate trends along isotherms in CO_2 and the CO_2 gas mixtures. However the rate constants in Table III are calculated from the cubic fit (Eq. (14)) to the weight loss data. The different isotherms are represented by the following symbols: ●, 390°C; ▽, 416°C; ▼, 470°C; □, 500°C; and ■, 530°C.

(1966) reported an activation energy of 112 kJ mole^{-1} for pyrite decomposition at 468–578°C in vacuum. Finally, a cubic fit using Eq. (14) to the BU data (Table I) for pyrite decomposition in pure CO_2 gives an activation energy of 141 ± 8 kJ mole^{-1} in good agreement with the other data sets. The activation energy plot for the BU data is shown in Fig. 11.

Our experiments lead to several important conclusions. First, the experiments confirm one part of the hypothesized sulfur cycle, namely the production of reduced sulfur gases via pyrite chemical weathering on the surface of Venus. Originally, pyrite chemical weathering was hypothesized to take place via direct oxidation to magnetite accompanied by the release of reduced sulfur gases (Von Zahn *et al.* 1983, Prinn 1985). However, as discussed above and illustrated in Fig. 4 and 6, our experiments show that pyrite first thermally decomposes to low-Fe pyrrhotite (Fe_7S_8), which loses sulfur to form more Fe-rich pyrrhotite (Fe_9S_{10}). The pyrrhotite also undergoes oxidation to magnetite, which in turn is oxidized to maghemite, which then converts to hematite.

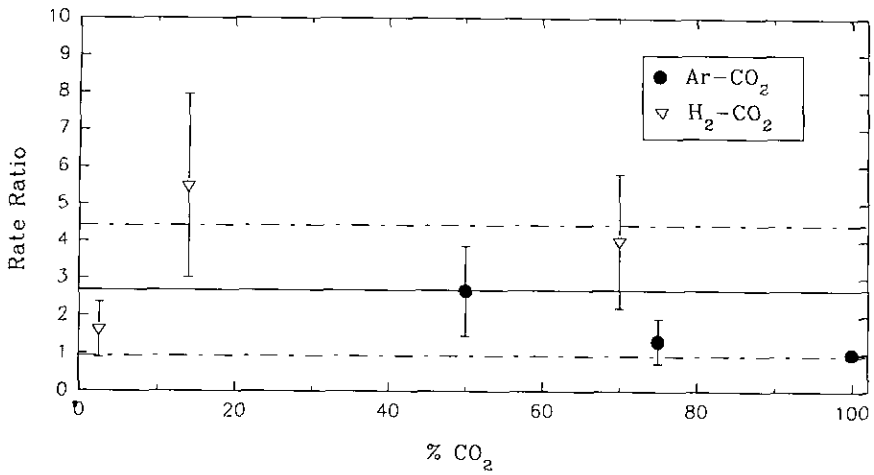

FIG. 10. Normalized rate constants in Ar–CO_2 and H_2–CO_2 gas mixtures are compared to the rate constant in pure CO_2. The solid horizontal line is the mean of the normalized rate constants and the dashed horizontal lines are the 1σ uncertainties on the mean.

The pyrite → low-Fe pyrrhotite → high-Fe pyrrhotite steps in our scheme are supported by several prior experimental studies. Jagadeesh and Seehra (1981) made thermomagnetic measurements and showed that pyrite heated at 485°C in He forms monoclinic pyrrhotites in the range of $Fe_{0.87-0.89}S$. However they did not heat samples long enough to produce high-Fe pyrrhotites. Hoare *et al.* (1988) heated pyrite in N_2 from 427 to 927°C and reported that Fe_7S_8 formed and then decomposed to more Fe-rich pyrrhotites. Safiullin and Gitis (1968) heated pyrite in Ar at 660–800°C and found more Fe-rich pyrrhotites on longer heating and at higher temperatures. The pyrrhotite → magnetite → maghemite → hematite steps in our scheme are also supported by prior experimental studies. Asaki *et al.* (1983) found that troilite oxidizes to magnetite in Ar–O_2 mixtures at 750–850°C, and that the magnetite then oxidizes to hematite. As noted earlier, a number of workers showed that magnetite oxidation to hematite occurs via maghemite formation over the temperature range we studied (e.g., Colombo *et al.* 1965, Davis *et al.* 1968, Elder 1965, Feitknecht and Gallagher 1970, Feitknecht and Mannweiler 1967, Gallagher *et al.* 1968, Johnson and Jensen 1974, Kachi *et al.* 1963, Özdemir and Banerjee 1984, Özdemir and Dunlop 1989). Hagni *et al.* (1992) studied air-roasted pyrite particles by reflected light microscopy and showed (their Fig. 1) a pyrite particle that was partially reacted at 500°C and is coated by sequential layers of pyrrhotite, magnetite, and hematite. They also noted that the pyrrhotite has a radial fibrous structure, which is very similar to what we observe in our samples (e.g., see the photographs in Fig. 4).

Second, the pyrite lifetimes listed in Table III for the CO_2–CO–SO_2 gas mixture show that the rate of pyrite destruction on the surface of Venus varies from about 1225 ± 238 days/cm at the top of Maxwell Montes (~660 K) to about 233 ± 133 days/cm in the plains of Venus (~740 K). These lifetimes are very short on a geological time scale and show that pyrite cannot exist on the surface of Venus for any appreciable length of time. Even decameter-sized masses of pyrite will be destroyed on ~3300-year time scales at the top of Maxwell and much more rapidly in the plains. Thus, pyrite cannot be present on the surface of Venus for any length of time and it is implausible that pyrite is the cause of the low-emissivity regions seen in the Pioneer Venus and Magellan radar observations (Pettengill *et al.* 1982, 1988, 1991). If pyrite were buried on Venus, then the diffusion of S_2 vapor through the overlying rock may become the rate-controlling step. However, then the pyrite could not be observed by the centimeter wavelength radar used on the Pioneer Venus and Magellan spacecraft and could not be causing the low emissivity. In fact, several alternative models, which do not involve pyrite, have been proposed to explain the low-emissivity regions in the highlands of Venus (Shepard *et al.* 1994, Brackett *et al.* 1994, 1995, Tryka and Muhleman 1992, Pettengill *et al.* 1992).

Finally, another important conclusion from our experiments is that the rate of pyrrhotite oxidation on Venus is significantly slower than the rate of pyrite thermal decomposition. The fine-grained pyrrhotite produced in our experiments is oxidized to magnetite during the course of a run because pyrrhotite oxidation is a diffusion-controlled process that depends on particle size (e.g., Asaki *et al.* 1983, Treiman and Fegley 1991). The preliminary rate data for pyrrhotite oxidation (Treiman and Fegley 1991) predict that millimeter-sized pyrrhotite grains oxidize completely in hundreds of years, while decameter-sized masses of pyrrhotite, such as occur on the Earth in magmatic sulfide deposits, have lifetimes of millions of years on the surface of Venus. Thus our experiments predict

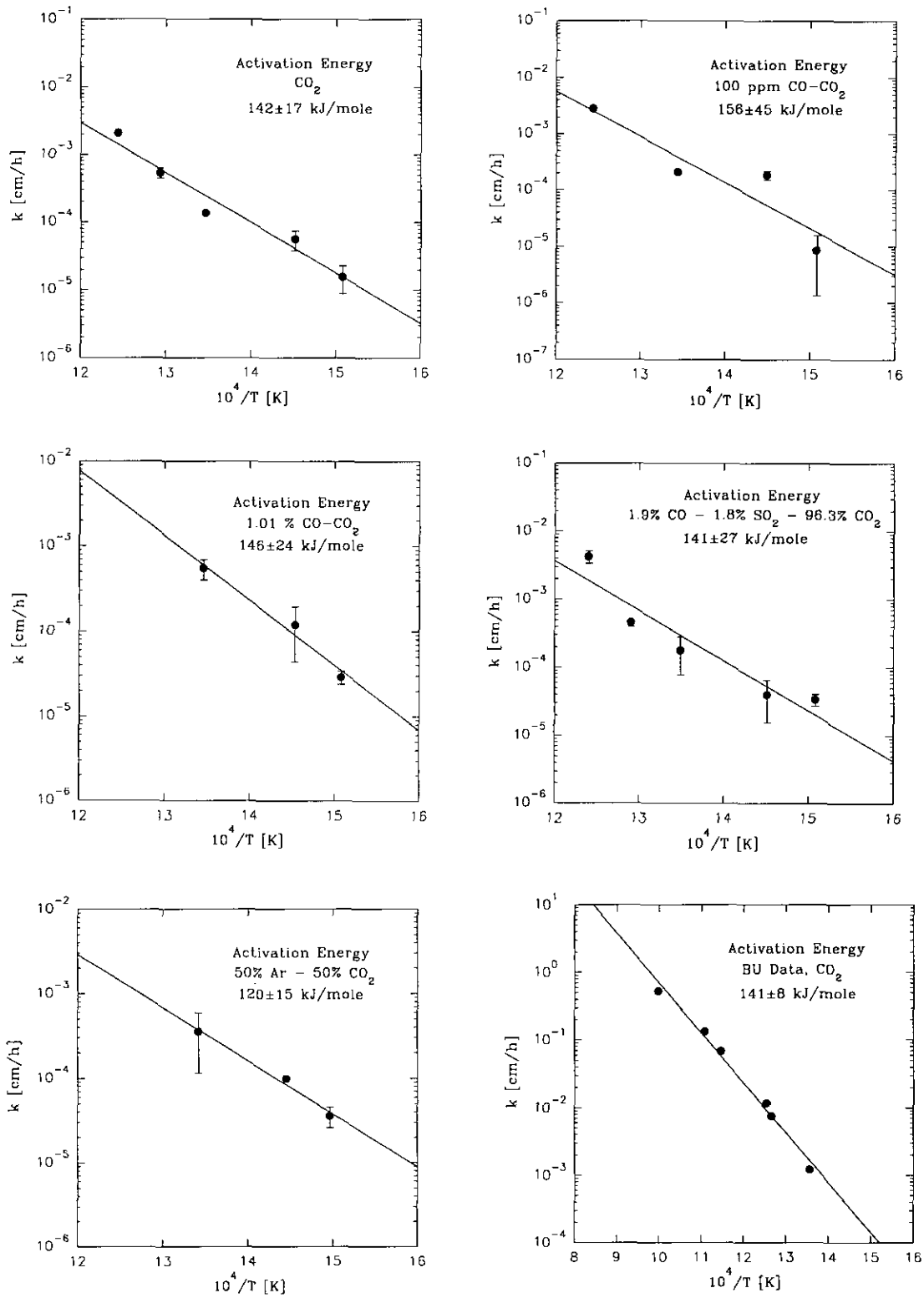

FIG. 11. Arrhenius plots for the rate constants from WU data in pure CO_2, 100 ppm $CO-CO_2$, 1.01% $CO-CO_2$, 50% Ar–50% CO_2, and 1.9% CO–1.8% SO_2–CO_2 over the range 390–530°C, and from Bu data in pure CO_2 and H_2–CO_2 over the 464–728°C range. The data in the plots are from cubic fits (Eq. (14)) to the weight loss data in Tables I and II.

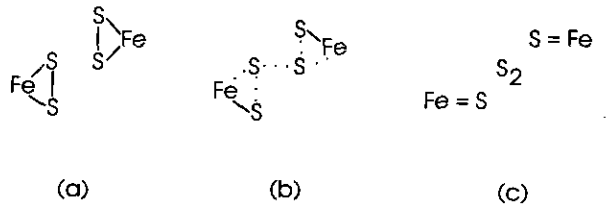

FIG. 12. A cartoon showing our proposed rate-determining step for pyrite thermal decomposition to pyrrhotite. (a) Fe–S bonds in pyrite. (b) The transition state formed in the rate-determining step, which is a release of S_2 vapor. (c) Release of S_2 and Fe=S bonds in pyrrhotite.

that large pyrrhotite masses can exist for long time periods on the surface of Venus. The presence of pyrrhotite, which is a source of COS via oxidation by atmospheric CO_2 and CO (Fegley and Treiman 1992), is supported by the observed increase of COS with decreasing altitude on Venus (Pollack *et al.* 1993).

ACKNOWLEDGMENTS

We thank D. Kremser and R. Poli from Washington University, B. Spettel from the Max Planck Institute in Mainz, P. Held from the Technische Hochschule, Darmstadt, and J. Fox at Ward's Scientific for their assistance; the Harvard Mineralogical Museum and Boston University for pyrite samples; R. E. Arvidson, R. A. Brackett, J. Bergstralh, D. Hunten, D. Kremser, and K. Burke for informal reviews of the manuscript; and J. Kargel and S. D. Scott for formal reviews of the manuscript. The work at Washington University was supported by Grant NAGW-2867 from the NASA Planetary Atmospheres Program (B. Fegley, P.I.) The collaborative work between Washington University and the Technische Hochschule, Darmstadt is made possible by NATO Collaborative Research Grant 931476.

REFERENCES

ARNOLD, R. G. 1969. Pyrrhotite phase relations below 304 ± 6°C at <1 atm total pressure. *Econ. Geol.* **64,** 405–419.

ASAKI, Z., K. MATSUMOTO, T. TANABE, AND Y. KONDO 1983. Oxidation of dense iron sulfide. *Metall. Trans B* **14,**109–116.

BANDO, Y., M. KIYAMA, T. TAKADA, AND S. KACHI 1965. The effect of particle size of γ-Fe_2O_3 and the transformation from γ-form to α-form. *Jpn. J. Appl. Phys.* **4,** 240–241.

BOG, S., AND T. ROSENQVIST 1959. A high-temperature manometer and the decomposition pressure of pyrite. *Trans. Faraday Soc.* **55,** 1565–1569.

BRACKETT, R. A., B. FEGLEY JR., AND R. E. ARVIDSON 1994. Vapor transport, weathering, and the highlands of Venus. *Lunar Planet. Sci. XXV,* 157–158.

BRACKETT, R. A., B. FEGLEY, JR., AND R. E. ARVIDSON 1995. Volatile transport on Venus and implications for surface geochemistry and geology. *J. Geophys. Res. Planets,* **100,** 1553–1563.

BROWN, M. E., D. DOLLIMORE, AND A. K. GALWEY 1980. Theory of solid state reaction kinetics. In *Comprehensive Chemical Kinetics Reactions in the Solid State* (C. H. Bamford and C. F. H. Tipper, Eds.), Vol. 22, pp. 41–113. Elsevier Scientific, Amsterdam.

CALVO, M., AND E. SEVILLANO 1989. Pyrite crystals from Soria and La Rioja provinces Spain. *Mineral. Rec.* **20,** 451–456.

CLARK, A. H. 1966. Stability field of monoclinic pyrrhotite. *Inst. Min. Metal. Trans.* **75B,** 232–235.

COATS, A. W., AND N. F. H. BRIGHT 1966. The kinetics of the thermal decomposition of pyrite. *Can. J. Chem.* **44,** 1191–1195.

COLOMBO, U., F. GAZZARRINI, G. LANZAVECCHIA, AND G. SIRONI 1965. Magnetic oxidation: A proposed mechanism. *Science* **147,** 1033.

CORLETT, M. 1968. Low-iron polymorphs in the pyrrhotite group. *Z. Kristallogr.* **126,** 124–134.

DAVID, I., AND A. J. E. WELCH 1956. The oxidation of magnetite and related spinels. *Trans. Faraday. Soc.* **52,** 1642–1650.

DAVIS, B. L., G. RAPP, AND M. J. WALAWENDER 1968. Fabric and structural characteristics of the martitization process. *Am. J. Sci.* **266,** 482–496.

DEER, W. A., R. A. HOWIE, AND J. ZUSSMAN 1963. *Rock-Forming Minerals.* Wiley, New York.

DEGRAVE, E., AND A. VAN ALBOOM 1991. Evaluation of ferrous and ferric Mössbauer fractions. *Phys. Chem. Miner.* **18,** 337–342.

DESBOROUGH, G. A., AND R. H. CARPENTER 1965. Phase relations of pyrrhotite. *Econ. Geol.* **60,** 1431–1450.

ELDER, T. 1965. Particle-size effect in oxidation of natural magnetite. *J. Appl. Phys.* **36,** 1012–1013.

FEGLEY, B., JR., G. KLINGELHÖFER, R. A. BRACKETT, AND N. IZENBERG 1994a. The oxidation state of the surface of Venus. *Meteoritics* **29,** 465–466.

FEGLEY, B., JR., G. KLINGELHÖFER, AND K. LODDERS 1994b. The formation of hematite on the surface of Venus. *Bull. Am. Astron. Soc.* **26,** 1145.

FEGLEY, B., JR., AND K. LODDERS 1993a. The rate of chemical weathering of pyrite on the surface of Venus. *Lunar Planet. Sci. XXIV,* 467–468.

FEGLEY, B., JR., AND K. LODDERS 1993b. Experimental studies of the rate of pyrite decomposition on the surface of Venus. *EOS Trans. Am. Geophys. Union* **74,** 190.

FEGLEY, B., JR., K. LODDERS, AND G. KLINGELHÖFER 1993. Kinetics and mechanism of pyrite decomposition on the surface of Venus. *Bull. Am. Astron. Soc.* **25,** 1094.

FEGLEY, B., JR., AND R. G. PRINN 1989. Estimation of the rate of volcanism on Venus from reaction rate measurements. *Nature* **337,** 55–58.

FEGLEY, B., JR., AND A. H. TREIMAN 1991. Venus: First experimental measurements of the rate of pyrite FeS_2 chemical weathering. *Bull. Am. Astron. Soc.* **22,** 1055.

FEGLEY, B., JR., AND A. H. TREIMAN 1992. Chemistry of atmosphere–surface interactions on Venus and Mars. In *Venus and Mars: Atmospheres, Ionospheres, and Solar Wind Interactions* (J. G. Luhmann, M. Tatrallyay, and R. O. Pepin, Eds.), pp. 7–71. American Geophysical Union, Washington, DC.

FEITKNECHT, W., AND K. J. GALLAGHER 1970. Mechanisms for the oxidation of Fe_3O_4. *Nature* **228,** 548–549.

FEITKNECHT, W., AND U. MANNWEILER 1967. Der Mechanismus der Umwandlung von γ- zu α-Eisensesquioxid. *Helv. Chim. Acta* **50,** 570–581.

FYSH, S. A. 1986. Mössbauer spectroscopy as a tool for studying hydrometallurgical treatments of copper-iron sulfides. In *Industrial Applications of the Mössbauer Effect* (G. J. Long and J. G. Stevens, Eds.). Plenum Press, New York.

GALLAGHER, K. J., W. FEITKNECHT, AND U. MANNWEILER 1968. Mechanism of oxidation of magnetite to γ-Fe_2O_3. *Nature* **217,** 1118–1121.

GILLSON, J. L. 1927. Origin of the Vermont talc deposits, with a discussion on the formation of talc in general. *Econ. Geol.* **22,** 246–285.

GREENWOOD, N. N., AND T. C. GIBB 1971. *Mössbauer Spectroscopy.* Chapman and Hall, London.

GRØNVOLD, F., AND H. HARALDSEN 1952. On the phase relations of synthetic and natural pyrrhotites. *Acta Chem. Scand.* **6,** 1452–1459.

HAGNI, A. M., R. D. HAGNI, AND P. R. TAYLOR 1992. Mineralogical and textural characterization of lime roasted pyrite and arsenopyrite for gold leaching. In *EPD Congress 1993* (J. P. Hager, Ed.), pp. 393–401. Minerals, Metals, and Materials Society, Warrendale, PA.

HELD, P., R. TEUCHER, G. KLINGELHÖFER, J. FOH, H. JÄGER, AND E. KANKELEIT 1993. A Mössbauer spectrometer for the mineralogical analysis of the Mars surface: First temperature dependent tests of the detector and drive system. *Lunar Planet. Sci. XXIV,* 633–634.

HOARE, I. C., H. J. HURST, W. I. STUART, AND T. J. WHITE 1988. Thermal decomposition of pyrite. *J. Chem. Soc. Faraday Trans. I* **84,** 3071–3077.

HUEBNER, J. S. 1987. Use of gas mixtures at low pressure to specify oxygen and other fugacities of furnace atmospheres. In *Hydrothermal Experimental Techniques* (G. C. Ulmer and H. L. Barnes, Eds.), pp. 20–60. Wiley, New York.

JAGADEESH, M. S., AND M. S. SEEHRA 1981. Thermomagnetic studies of conversion of pyrite and marcasite in different atmospheres (vacuum, H_2, He, and CO). *J. Phys. D.* **14,** 2153–2167.

JOHNSON, H. P., AND S. D. JENSEN 1974. High temperature oxidation of magnetite to maghemite. *EOS Trans. Am. Geophys. Union* **55,** 233.

KACHI, S., K. MOMIYAMA, AND S. SHIMIZU 1963. An electron diffraction study and a theory of the transformation from γ-Fe_2O_3 to α-Fe_2O_3. *J. Phys. Soc. Jpn* **18,** 106–116.

KANKELEIT, E. 1964. Velocity spectrometer for Mössbauer experiments. *Rev. Sci. Instrum.* **35,** 194–197.

KANKELEIT, E., J. FOH, P. HELD, G. KLINGELHÖFER, AND R. TEUCHER 1994. A Mössbauer experiment on Mars *Hyperfine Interact.* **90,** 107–120.

KISSIN, S. A., AND S. D. SCOTT 1982. Phase relations involving pyrrhotite below 350°C. *Econ. Geol.* **77,** 1739–1754.

KLINGELHÖFER, G., B. FEGLEY, JR., AND K. LODDERS 1994. ^{57}Fe Mössbauer studies of the kinetics of pyrite decomposition on the surface of Venus. *Lunar Planet. Sci. XXV,* 707–708.

KLINGELHÖFER, G., J. FOH, P. HELD, H. JÄGER, E. KANKELEIT, AND R. TEUCHER 1992. Mössbauer backscattering spectrometer for mineralogical analysis of the Mars surface. *Hyperfine Interact.* **71,** 1449–1452.

KRUSE, O. 1990. Mössbauer and X-ray study of the effects of vacancy concentration in synthetic hexagonal pyrrhotites. *Am. Mineral.* **75,** 755–763.

KUBASCHEWSKI, O., C. B. ALCOCK, AND P. J. SPENCER 1993. *Materials Thermochemistry,* 6th ed. Pergamon Press, Oxford.

KULLERUD, G., AND H. S. YODER 1959. Pyrite stability relations in the Fe–S system. *Econ. Geol.* **54,** 533–572.

MEISEL, W., P. GRIESBACH, H. J. GRABKE, AND P. GÜTLICH 1990. Quantitative determination of fayalite layers on iron by CEMS. *Hyperfine Interact.* **57,** 2001–2008.

MORIMOTO, N., A. GYOBU, H. MUKAIYAMA, AND E. IZAWA 1975. Crystallography and stability of pyrrhotites. *Econ. Geol.* **70,** 824–833.

MORIMOTO, N., AND H. NAKAZAWA 1968. Pyrrhotites: Synthetics having two new superstructures. *Science* **161,** 577–579.

NAKAZAWA, H., AND N. MORIMOTO 1970. Pyrrhotite phase relations below 320°. *Proc. Jpn. Acad.* **46,** 678–683.

NAKAZAWA, H., AND N. MORIMOTO 1971. Phase relations and structures of pyrrhotite $Fe_{1-x}S$. *Mater. Res. Bull.* **6,** 345–358.

O'NEILL, H. ST. C. 1988. Systems Fe–O and Cu–O: Thermodynamic data for the equilibria Fe–"FeO," Fe–Fe_3O_4, "FeO"–Fe_3O_4, Fe_3O_4–Fe_2O_3, Cu–Cu_2O, and Cu_2O–CuO from emf measurements. *Am. Mineral.* **73,** 470–486.

ÖZDEMIR, Ö., AND S. K. BANERJEE 1984. High temperature stability of maghemite (γ-Fe_2O_3) *Geophys. Res. Lett.* **11,** 161–164.

ÖZDEMIR, Ö., AND D. J. DUNLOP 1989. Chemico-viscous remanent magnetization in the Fe_3O_4–γFe_2O_3 system. *Science* **243,** 1043–1047.

PANNETIER, G., AND L. DAVIGNON 1961. Étude de la décomposition thermique sous vide du sulfure de fer FeS_2 et du sulfure de cobalt CoS_2. *Bull. Soc. Chim.,* 1513–1517.

PETTENGILL, G. H., P. G. FORD, AND B. D. CHAPMAN 1988. Venus: Surface electromagnetic properties. *J. Geophys. Res.* **93,** 14881–14892.

PETTENGILL, G. H., P. G. FORD, W. T. K. JOHNSON, P. K. RANEY, AND L. A. SODERBLOM 1991. Magallan: Radar performance and data products. *Science* **252,** 260–265.

PETTENGILL, G. H., P. G. FORD, AND S. NOZETTE 1982. Venus: Global surface radar reflectivity. *Science* **217,** 640–642.

PETTENGILL, G. H., P. G. FORD, AND R. J. WILT 1992. Venus surface radiothermal emission as observed by Magellan. *J. Geophys. Res.* **97,** 13091–13102.

PIETERS, C. M., J. W. HEAD, W. PATTERSON, S. PRATT, J. GARVIN, V. L. BARSUKOV, A. T. BASILEVSKY, I. L. KHODAKOVSKY, A. S. SELIVANOV, A. S. PANFILOV, YU. M. GEKTIN, AND Y. M. NARAYEVA 1986. The color of the surface of Venus. *Science* **234,** 1379–1383.

POLLACK, J. B., B. DALTON, D. H. GRINSPOON, R. B. WATTSON, R. FREEDMAN, D. A. CRISP, B. BEZARD, C. DEBERGH, L. GIVER, Q. MA, AND R. TIPPING 1993. Near-infrared light from Venus' nightside: A spectroscopic analysis. *Icarus* **103,** 1–42.

PRINN, R. G. 1985. The photochemistry of the atmosphere of Venus. In *The Photochemistry of Atmospheres* (J. S. Levine, Ed.), pp. 281–336. Academic Press, New York.

SAFIULLIN, N. SH., AND E. B. GITIS 1968. Thermochemical conversions of iron pyrite and pyrrhotite on heating in oxidizing and inert media. *J. Appl. Chem. USSR* **41,** 1596–1602.

SAMAL, G. I. 1966. Kinetics of the thermal decomposition of iron disulfide. *Geterog. Khim. Reakts. Inst. Obshch. Neorg. Khim. Akad. Nauk Belorussk. SSR,* 93–99 (1965), cited in *Chem. Abstracts* **64,** 15048d.

SCHWAB, G. M., AND J. PHILINIS 1947. Reactions of iron pyrite: Its thermal decomposition, reduction by hydrogen and air oxidation. *J. Am. Chem. Soc.* **69,** 2588–2596.

SCHWERDTFEGER, K., AND E. T. TURKDOGAN 1970. Chemical Equilibria. In *Techniques of Metals Research* (R. A. Rapp, Ed.), Vol. IV, pp. 321–407. Wiley, New York.

SHEPARD, M. K., R. E. ARVIDSON, R. A. BRACKETT, AND B. FEGLEY JR. 1994. A ferroelectric model for the low emissivity highlands on Venus. *Geophys. Res. Lett.* **21,** 469–472.

TAYLOR, L. A. 1970. Low-temperature phase relations in the Fe–S system. *Carnegie Inst. Washington Year Book* **68,** 259–270.

TOULMIN III, P., AND BARTON, P. B. 1964. A thermodynamic study of pyrite and pyrrhotite. *Geochim. Cosmochim. Acta* **28,** 641–671.

TREIMAN, A. H., AND B. FEGLEY, JR. 1991. Venus: The chemical weathering of pyrrhotite $Fe_{1-x}S$. *Lunar Planet Sci. XXII,* 1409–1410.

TRYKA, K. A., AND D. O. MUHLEMAN 1992. Reflection and emission properties on Venus: Alpha Regio. *J. Geophys. Res.* **97,** 13379–13394.

VAUGHAN, D. J., AND J. R. CRAIG 1978. Mineral chemistry of metal sulfides. Cambridge Univ. Press, Cambridge.

VON ZAHN, U., S. KUMAR, H. NIEMANN, AND R. G. PRINN 1983. Composition of the Venus atmosphere. In *Venus* (D. M. Hunten, L. Colin, T. M. Donahue, and V. I. Moroz, Eds.), pp. 299–430. Univ. of Arizona Press, Tucson.

YUND, R. A., AND H. T. HALL 1969. Hexagonal and monoclinic pyrrhotites. *Econ. Geol.* **64,** 420–423.

ZHUKOVSKII, V. M., I. A. MONTILO, AND A. A. BABADZHAN 1967. Thermal decomposition of pyrite. *Tr. Ural. Nauchno. Issled. Proektn. Inst. Mednoi Prom.* No. 8, 387–390 (1965) cited in Chem. Abstracts **66,** 108758e.